MINING-INDUCED SEISMICITY AND FLAC3D MODELING AT THE TRAIL MOUNTAIN MINE

by

Meagan Shawn Boltz

A thesis submitted to the faculty of
The University of Utah
in partial fulfillment of the requirements for the degree of

Master of Science

Department of Mining Engineering

The University of Utah

December 2014

The University of Utah Graduate School

STATEMENT OF THESIS APPROVAL

The following faculty members served as the supervisory committee chair and members for the thesis of Meagan Shawn Boltz. Dates at right indicate the members' approval of the thesis.

Michael K. McCarter, Chair	08/11/14 Date Approved
Kristine L. Pankow, Co-Chair	08/11/14 Date Approved
Zavis M. Zavodni, Member	08/11/14 Date Approved

The thesis has also been approved by Michael G. Nelson

Chair of the Department/School/College of Mining Engineering

and by David B. Kieda, Dean of The Graduate School.

ABSTRACT

Mining-induced seismicity (MIS) is unpredictable and has the potential to be damaging; therefore, it is important to study it to gain insight into how rock damage develops in a mine. A dataset of 1906 mining-induced events was recorded at the Trail Mountain Mine (TMM). These events cluster on Panel 13, the active panel during data collection. In this thesis, a $FLAC^{3D}$ model of the mine was developed to determine if there are correlations between the seismicity and selected parameters from the model.

A model of a single longwall panel indicates that stresses in the model have an error of approximately 12.5% due to limitations in the approach used to represent joints. Subsidence in the model closely matches the subsidence measured at the mine, indicating that the model captures the first-order behavior of the mine. High stress areas in the model occur on the gateroads with increasing stress toward the east side of the workings. Peaks in the maximum shear stress are followed by peaks in seismic moment, which is consistent with seismicity accompanying de-stressing in the rock mass. Some features of the seismicity could not be explained by the model, such as the cluster at the end of the panel, which is thought to have been caused by factors that were not included in the model. The model also cannot account for the absence of floor events. The reason for the difference is unclear, but it indicates that stresses alone are not a sufficient indicator of the potential for MIS. Failed zones in the model were compared with the locations and moments of the seismicity recorded on Panel 13 and were not found to relate to the seismicity.

The results of this study indicate that the model is not yet sophisticated enough to understand the seismicity at the TMM, likely because several features of the mine that could potentially explain the seismicity, such as near-seam geology and older mine workings, were not included. This model serves as a foundation for future research on seismicity at the TMM and provides insight in how to develop similar models for other mines.

TABLE OF CONTENTS

LIST OF FIGURES

FIGURE PAGE

ACKNOWLEDGEMENTS

I would like to thank my advisor, Dr. Michael K. McCarter, for his guidance during my graduate work and for getting me involved in research. I would also like to thank Dr. Kristine L. Pankow for her support and mentorship as well as for serving on my committee. I want to acknowledge Dr. Zavis M. Zavodni for serving on my committee.

I would like to thank Dr. William Pariseau for his mentorship regarding numerical modeling. I am also grateful for the input from Dr. Keith Koper, Katherine Whidden, Tex Kubacki, Derrick Chambers, Jessica Wempen, and Jared Stein.

I am grateful to Itasca Consulting Group for allowing me to be a part of their mentorship program during the course of my research, and I am especially grateful to Dr. Ed Dzik for serving as my mentor and providing me with valuable advice for working with *FLAC*^{3D}. I would also like to thank Itasca Consulting Group for allowing me access to their longwall modeling environment.

I thank NIOSH for providing funding for this research (Contract Number 200-2011-39614) . I thank Energy West Mining Company, a subsidiary of PacifiCorp, for providing information about the Trail Mountain Mine.

Finally, I would like to thank my family for all of their support during my schooling as well as the Perkes family for getting me involved in mining engineering and for all of their support over the years. Thank you also to Ed Bolton for being a friend when times were tough.

The views and conclusions contained in this document are those of the author and should not be interpreted as representing the opinions or policies of NIOSH or other supporters of this research.

1. INTRODUCTION

1.1. Problem Statement

Mining-induced seismicity (MIS) has been a prevalent issue in underground coal mining for many years. MIS is a phenomenon where seismic events occur as a result of changes in stress and strain in the rock mass due to the excavation of material. Several factors may influence the generation of MIS, including: geology, depth of cover, in-situ stress, and mining method (Iannacchione and Zelanko 1995). Seismicity that is directly related to mining is shallow and often located near mine workings with locations corresponding to geological and mechanical zones of weakness around the mine (Johnston 1992). These events are typically small in magnitude ($M < 3$), and the number of events is related to mining advance. The seismic activity can be in the form of ground shaking with no observed damage, or it may consist of violent expulsions of rock, known as rockbursts or bumps. It is difficult to determine which events are going to be damaging (Mark 2012); therefore, it is important to study MIS to gain insight into how rock damage develops in a mine. There has been considerable previous research studying MIS (see Gibowicz (2009) and Gibowicz and Lasocki (2001) for a review of MIS research), but exact relations between the mining process and MIS remain largely unknown.

A dataset was collected by the University of Utah Seismograph Stations at the Trail Mountain Mine (TMM), which has been extensively studied and relocated (Arabasz et al. 2002; Arabasz et al. 2005; Boltz et al. 2012; Boltz et al. 2014). Seismicity was

recorded from October 2000 to April 2001 at the mine using a temporary seismic array. While the array was deployed, part of Panel 12 and all of Panel 13 were extracted (Figure 1.1a). Panel 12 was abandoned after excavating 350 m due to excessive seismicity, and the unmined portion of the panel was left as a barrier between Panel 13 and the older workings to the south. Approximately 1900 MIS events were recorded at the mine during the time of the experiment. The events were relocated using multiple techniques described in Boltz et al. (2014), and the preferred locations for the seismicity are shown in Figures 1.1a and 1.1b. The locations have good epicentral resolution, with the seismicity coinciding closely with the mine workings. The locations also have good hypocentral resolution with the events appearing to occur in the mine roof with depth errors on the order of several hundred meters. It was not possible to obtain exact locations for the events; however, the locations are constrained enough to determine where the seismicity occurs relative to the mine, which can be used to further explore MIS and its causes.

While locating the MIS at the TMM, it was observed that the seismicity appeared to cluster on certain areas of Panel 13 (Figure 1.1a). The seismicity clusters along the gateroads over most of the panel, with the cluster on the tailgate containing more events than the cluster on the headgate. There is also a significant increase in the number of events per day (herein referred to as the seismicity rate) at the end of the panel, followed by the seismicity merging to form a single cluster across the panel. It is hypothesized that the formation of these clusters may be influenced by areas of high stress concentration in the mine workings. For instance, the large cluster on the tailgate of Panel 13 may be due to the tailgate supporting the abutment of older mine workings in

addition to Panel 13, despite the presence of a barrier pillar between Panel 13 and these workings. Factors such as the depth of cover, geology, or the presence of older workings may have increased stress at the end of the panel and caused the increased seismicity rate.

A recommended method for developing a better understanding of MIS involves the integration of the analysis of seismic events with numerical modeling (Gibowicz 2009). There have been a growing number of studies that have successfully applied numerical modeling techniques to longwall mining (e.g., Badr et al. 2003; Maleki 2005; Pariseau 2012). One common program applied to mining problems is *FLAC*^{3D} (Itasca 2013a), a finite difference program developed by the Itasca Consulting Group that is designed for geotechnical applications. The objective of this study was to develop a *FLAC*^{3D} model of the TMM and determine if there is a correlation between selected model parameters (failed regions and high stress areas on Panel 13) and the locations of the MIS.

1.2. Trail Mountain Setting

The TMM is a longwall coal mine with a depth of cover ranging from 430 m to 670 m. Longwall operations were conducted at the mine from October 1995 to April 2001, following room and pillar operations on the east side of the mine. The TMM is located in the northwestern part of Emery County, Utah, approximately 45 km southwest of Price, Utah. The mine lies within the Wasatch Plateau coal field and is just east of the Joes Valley Reservoir. The Wasatch Plateau/Book Cliffs area is one area in the western United States where MIS is prevalent. Hundreds of mining events are recorded in the area each year (Ellenberger and Heasley 2000).

1.2.1. Geology

The Wasatch Plateau is one of a series of NNE-trending plateaus along the northwest rim of the Colorado Plateau that correspond to the transition between the Basin and Range and Colorado Plateau province (Arabasz et al. 2002). The plateau is 145 km in length in the north-south direction and 11–32 km wide in the east-west direction. The elevation of the plateau ranges from 1,980 m to 3,350 m (Jones 1994). The Wasatch Plateau is cut by a series of *en echelon* north-south trending grabens. The Joes Valley graben, which lies along the western edge of Trail Mountain, is structurally controlled by the Joes Valley fault zone, which consists of predominantly north-south striking normal faults that are nearly parallel to a dominant north-south joint set (Maleki 2005). Trail Mountain has flat-topped mesas on its upper surface at elevations that range from 2,600 m to greater than 3,000 m. Steep canyon walls resulting from erosional incision of the Wasatch Plateau form its southern and eastern sides.

Jointing around the TMM is moderately developed with major groups striking N10°E and N75°W in addition to several minor groups (Jones 1994; Maleki 2005). Joints are typically near-vertical with lengths of 12–76 m and spacing of 6–122 m (Maleki 2005). The jointing in the Wasatch Plateau has medium-to-high persistence, particularly for the north-south oriented set. Joints are mapped in all rock units.

The strata underlying Trail Mountain consist of sedimentary stratigraphic units that range from upper Cretaceous to Tertiary age and have a shallow westward dip (<5°) (Arabasz et al. 2002). The strata are made up of sandstones, shales, siltstones, mudstones, and coal that can be divided into seven major formations, described below (Figure 1.2).

1.2.1.1. Mancos Shale. The Mancos Shale is a massive marine shale. It is greater than 300 m thick, approaching 395 m near the TMM. Exposed portions of the shale are soft and well-weathered (Jones 1994).

1.2.1.2. Star Point Sandstone. The Star Point Sandstone is composed of massive fine-to-medium grained cliff-forming sandstones that are interbedded with the Mancos Shale and partings of thin-bedded sandstone (Doelling 1972). The unit is 75-106 m thick and is located beneath the shale and mudstone floor of the Hiawatha Coal Seam.

1.2.1.3. Hiawatha Coal Seam. The Hiawatha Coal Seam is the seam that was mined at the TMM. It is located at the base of the Blackhawk Formation and has several benches and partings with a mineable thickness of 2.6–4.1 m. The average mining height at the TMM is 2.7 m. The seam thickness to the north and mudstone partings near the roof can cause local stability problems to the south (Maleki 2005).

1.2.1.4. Blackhawk Formation. The Blackhawk Formation is 190 m to 245 m thick and contains interbedded layers of siltstones, mudstones, shale, sandstone, and coal (McCarter and McKenzie 2002). The layers in the Blackhawk Formation alternate between slope and cliff-forming layers that are less resistant than the surrounding sandstones. The material above the coal bed consists of braided stream deposits with lenticular sandstone channels that make up the immediate roof of mineable coal seams (Doelling 1972).

1.2.1.5. Castlegate Sandstone. The Castlegate Sandstone is a massive cliff-forming unit that consists of medium-to-coarse grained sandstone with occasional interbeds of hard shale and conglomerate. The thickness of this unit varies from 52–183 m (McCarter and McKenzie 2002).

1.2.1.6. Price River Formation. The Price River Formation is less resistant to erosion than the Castlegate Sandstone. The formation consists of coarse-grained sandstones with occasional interbeds of shale, pebble conglomerate, and mudstone that form step-like outcrops (Doelling 1972). The thickness of this unit ranges from 183–305 m.

1.2.1.7. North Horn Formation. The North Horn Formation contains interbeds of sandstone, siltstone, mudstone, and shale with increasing proportions of limestone near the top of the formation (Jones 1994). The contact between the North Horn Formation and Price River Formation is not obvious; however, the North Horn formation is redder and less resistant to erosion and forms slopes and rolling topography (Doelling 1972).

1.3. Longwall Mining Method

In the longwall mining method, large panels of coal (200–400 m wide, 1–4 km long, 1.5–6 m tall) are extracted. At the face of the panel, there is a shearer, a conveyor belt, and a row of shields that span the width of the panel. The shearer cuts the coal along the width of the panel at the free face. The shields, which separate the shearer and conveyor from the mined out area, serve to protect the workers and equipment, temporarily support the immediate roof, control the direction of caving, and walk the shearer forward. The shearer at the TMM advanced forward an average of 18 m/day. As the face advances, a void is left in its wake. By design, the roof of the panel caves and falls into this void, creating what is known as the gob.

The behavior of the roof as the gob is formed is ultimately unknown because it cannot be directly observed. One accepted description of the behavior in the roof is

provided by Singh and Kendorski (1981) and depicted in Figure 1.3. After a sufficient amount of material is extracted, induced stresses cause the material in the immediate roof to rubblize and fall into the void. This process progresses upward to approximately three to six times the mining height. The overlying strata break and slip along existing discontinuities. The fracturing progresses up another 24 to 54 times the mining height, or until the broken material bulks enough that overlying strata bend and come to rest on the gob material, but do not fracture. The bending of successive layers in the roof leads to the formation of a subsidence trough at the surface.

1.4. Scope of Thesis

The hypothesis of this thesis is that there are correlations between the results of a numerical model, specifically failed regions and stresses, and the locations and size of MIS recorded during the mining of Panel 13 at the TMM. In order to carry out this work, a model featuring the stratigraphy and topography around the TMM was developed using the finite difference software package, *FLAC*^{3D}. The model is based on a longwall modeling environment previously developed by Itasca Consulting Group (Pierce and Board 2010). It simulates the caving behavior in a longwall mine using the caving conceptual model of Singh and Kendorski (1981) and the relationship determined by Pappas and Mark (1993) to simulate the variation of the elastic modulus of the gob as it is formed and compacted. A three-dimensional code was selected for the modeling work because of the significant anisotropy around Panel 13 caused by a large variation in topography and the influence of old mine workings.

The modeling work was conducted in several steps. The appropriate behavior for the model was determined and a single longwall panel was excavated to verify that the

model functioned as expected. After the model was determined to function properly, a trial featuring the longwall panels on the west side of the TMM, herein referred to as a mine-wide analysis, was developed. The older panels were excavated to provide the initial stress state for Panel 13, as well as to evaluate the subsidence developed in the model. Panel 13 was then excavated in stages to simulate the advance of the panel. The accuracy of the model was evaluated by comparing the amount of subsidence generated in the model with the subsidence data recorded at the mine. A comparison was made between the failed zones in the model and the seismic moment of events that occurred to determine if the failed zones can be related to the seismic energy release. Finally, high stress areas in the mine were identified by examining vertical stress and maximum shear stress. Correlations between the high stress areas and locations of the seismicity were explored.

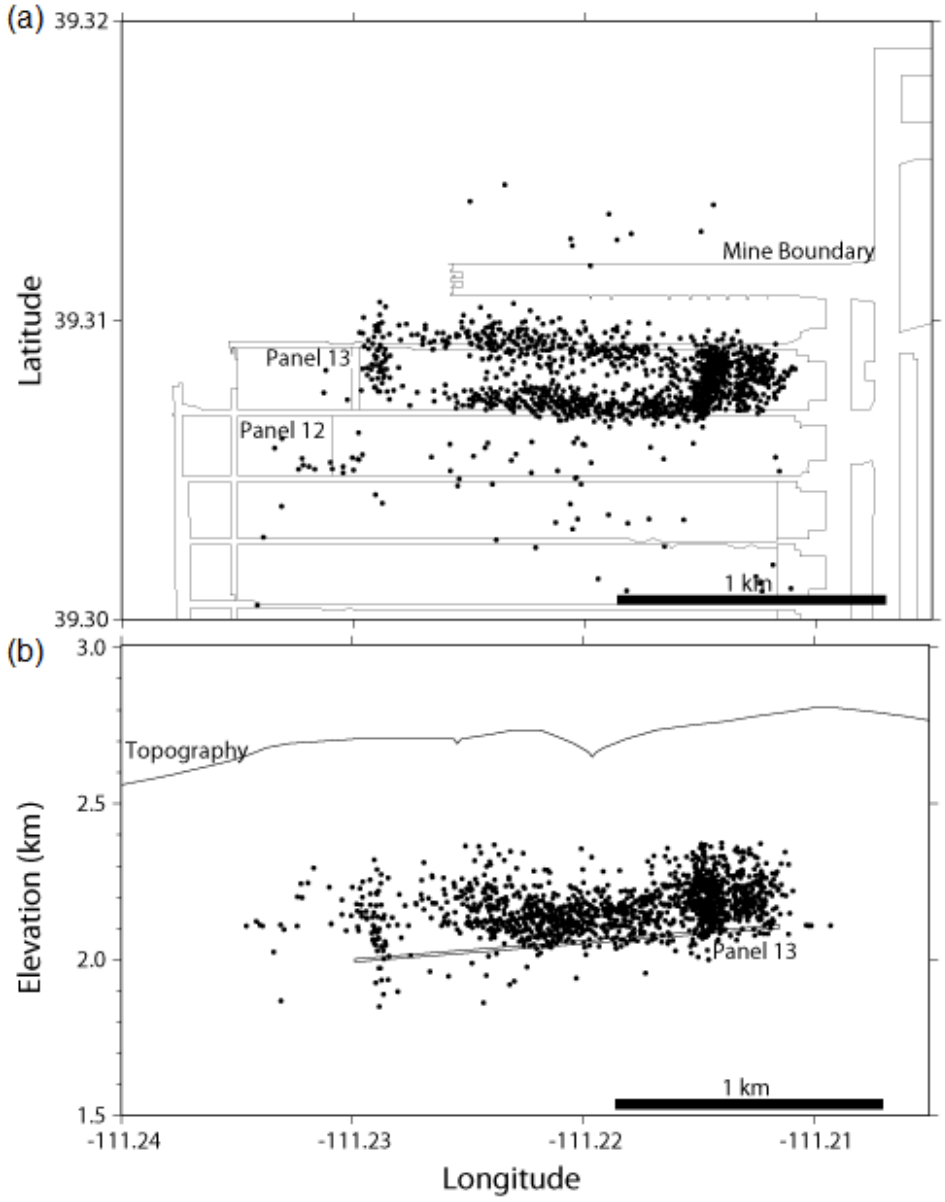

FIGURE 1.1 Preferred locations of seismicity at the Trail Mountain Mine from Boltz et al. (2014)

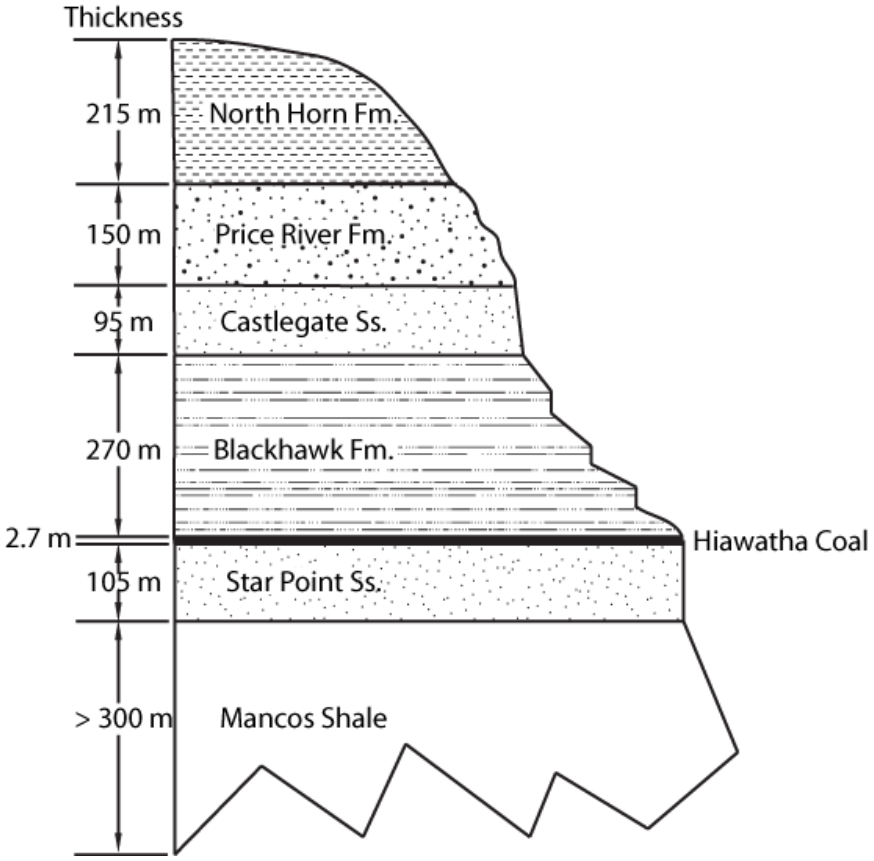

FIGURE 1.2 Stratigraphic column of Trail Mountain

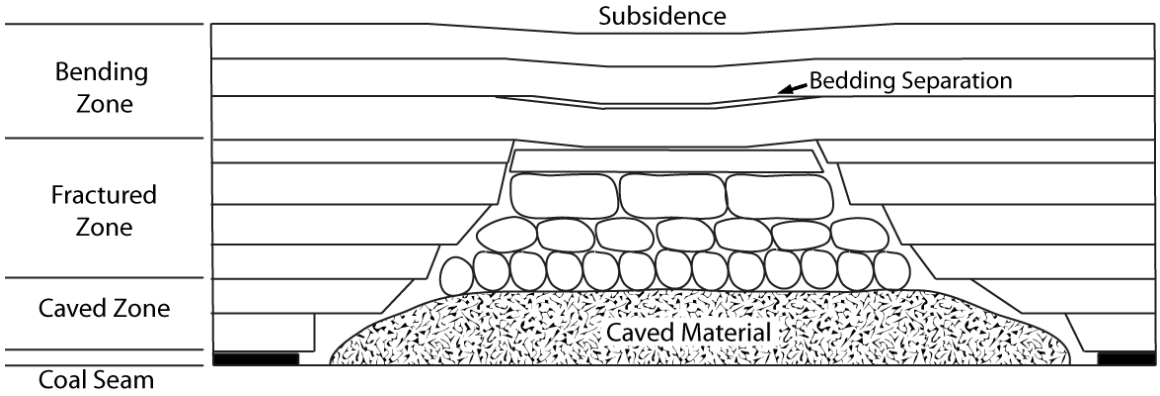

FIGURE 1.3 Diagram of caving developed during longwall mining, after Singh and Kendorski (1981)

2. RELATING SEISMICITY TO NUMERICAL MODELING

Relating numerical modeling with seismic data is a logical step in furthering the study of MIS. Currently, there is only limited research on relating these two elements. This chapter highlights previous methods that have been used to apply numerical modeling to the study of MIS. These methods include relating the stresses and energy release in the model to the location and energy of the seismic events.

One method of relating a static numerical model to seismic data is to qualitatively compare the locations of stress concentrations in the model with the locations of seismic events. This method has been successfully employed by Senfaute et al. (2001) and Wilson and Kneisley (1995). In Senfaute et al. (2001), seismic events were recorded at a longwall coal mine. The mine was modeled using a boundary element method. In their study, events located close to the area that was being actively mined, and the largest magnitude events occurred in the high stress areas that were identified in the model. Wilson and Kneisley (1995) modeled a longwall coal mine in Colorado using the displacement discontinuity program, MULSIM/PC. They observed that the stress across the panel face followed a pattern similar to the distribution of energy released by seismic events at the mine, with increased stress and energy both occurring on the tailgate. Mercer and Bawden (2005) observed that exploring correlations between stress and seismicity is a limited method because only weak linear relationships could be found between the two parameters. Furthermore, they indicate that while identifying high stress

areas using seismicity is possible, predicting the potential for seismicity from stresses is not as straightforward.

In addition to relating stress to seismicity, there are also studies that compare the energy released in a model with seismicity. Wiles (2005) back-analyzed a series of pillar bursts at a mine to develop a failure criterion for the energy density in a pillar and used it to determine whether a failing pillar would produce a rockburst and the amount of energy that the failure would release. A study by Spottiswoode et al. (2008) examined the energy release rate (ERR) calculated in models of two South African gold mines. They observed that the ERR correlates well with a number of seismic parameters, including number of events, seismic moment, and radiated energy. The ERR is a measure of the amount of strain energy that is released during failure divided by the area of a mined out region. An inherent difficulty in using energy to compare seismicity to modeling is that only a small part (<1%) of the elastic strain energy released during a failure is radiated as seismic energy (Spottiswoode et al. 2008), which raises the question of whether the total strain energy can be related to the seismic energy.

Another technique that has been used to relate numerical modeling to MIS is the excess shear stress (ESS) (Ryder 1987). Prior to the beginning of slip, a plane of weakness has a static strength that is made up of two parts: the cohesion of the material and the frictional resistance. After slip begins, the strength of the weakness plane reduces to a dynamic strength, which is only due to the frictional resistance to sliding. The reduction in strength results in a stress drop, known as the ESS, which is represented with the following equation:

$$ESS = |\tau| - \sigma_N \tan(\phi) \qquad \text{(EQ 2.1)}$$

where τ is the shear stress prior to slip, σ_N is the normal confining stress, and ϕ is the friction angle. Large values for the ESS (>20 MPa) are indicative of a rupture event. Maleki (2005) applied excess shear stress (ESS) to an elastic analysis of the TMM to estimate the locations and magnitudes of events at the mine. He observed that individual joints in the region were not large enough to produce MIS with magnitudes of the size observed at the TMM. He instead hypothesized that preexisting weakness planes in the rock mass could have coalesced to produce a larger discontinuity, which then slipped.

3. FLAC3D MODEL SETUP

The modeling work conducted in this study was conducted with the *FLAC*^{3D} software package. It was necessary to use a three-dimensional code for the model because the region around Panel 13, the panel of interest, is anisotropic due to the topography and presence of older mine workings. The code used to generate the model is based on a longwall modeling environment developed by the Itasca Consulting Group (Pierce and Board 2010), but has been adapted to better suit the conditions at the TMM. Specifically, changes have been made to incorporate the topography into the determination of the initial stress state, and logic has been modified to vary the moduli of zones that have caved. Changes have also been made to the way that joints are incorporated in the model. This chapter provides details of the structure and constitutive behavior of the model.

3.1. Grid

The grid for the model consists of the seven stratigraphic layers described in Section 1.2.1 with an embedded topographic surface (Figure 3.1). The strata around the TMM dip shallowly (<5°) to the west, but the dip is neglected because it would only have a small effect on the model results. The zones around the mine workings are evenly spaced and gradually become larger toward the boundary to reduce the size of the model. The zones for all layers except the Mancos Shale and Hiawatha Coal Seam are 14 m × 14 m × 14 m. The zones in the Mancos Shale are much coarser at 28 m × 28 m × 78 m, with

the longer dimension being in the vertical direction. The zones in the Hiawatha Coal Seam are 14 m × 14 m × 2.74 m to accommodate the height of the coal seam. The coal seam is only one element thick to maintain a reasonable model size; therefore, the model does not capture a detailed stress distribution through the coal seam. Zones surrounding the topographic surface are refined to more accurately reflect the topography.

A map of the TMM is shown in Figure 3.2. Panels 5–13, the panels on the west side of the mine, are the workings that are included in the model. Workings on the east side of the mine were excluded because including them would require doubling the size of the grid. The grid is too coarse to consider any workings other than the panels themselves. The mine geometry included in the model is shown in Figure 3.3. Each panel contains between 380 and 2,480 zones. The workings included in the model cover a 2,040 m × 2,100 m region. In order to minimize boundary effects, the modeled region is much larger. The grid is 6,030 m in the east-west direction, 6,280 m in the north-south direction, and varies in height from 553 m and 1,606 m. There are a total of 7.35 million zones and 8.40 million gridpoints.

3.2. Constitutive Behavior

The constitutive behavior for the model can be divided into three components: the behavior of the rock, behavior of the coal seam, and the behavior of the gob. The behavior is described in the following sections.

3.2.1. Rock

The rock layers above the mine are assigned the built-in Strain-Hardening/ Softening Ubiquitous-Joint (SUBI) constitutive model, which was developed by the

Itasca Consulting Group for modeling rock masses. When a zone fails, either the tensile strength or cohesion of the zone is reduced based on the failure mechanism and strain in the zone. The residual tensile strength of each zone is set to zero while the residual cohesion is set to 5% of the intact value. The strain at which the residual value is reached is based on an empirical relationship determined by Cundall et al. (2005) (from Pierce and Board 2010):

$$\varepsilon_{crit} = \frac{12.5 - 0.125 * \mathrm{GSI}}{100 * \mathrm{ZS}} \qquad \text{(EQ 3.1)}$$

where ε_{crit} is the residual strain, GSI is the geologic strength index, and ZS is the length of the sides of the zones in meters, assuming cube-shaped zones. The GSI for the strata are assumed to be 55. The model results are insensitive to the value used for the residual strain.

The layer immediately below the mine, the Star Point Sandstone, uses the Ubiquitous-Joint constitutive model and is unable to soften upon failure. The Mancos Shale, which is the bottommost layer in the model, is not expected to experience failure and was assigned an isotropic elastic constitutive model to reduce the size of the model.

3.2.2. Coal Seam

When a coal pillar takes on the load of the mined out area around it, the resulting stress distribution through the pillar is not uniform. Near the free faces of the pillar, there is less confinement, causing the strength to be lower. As a result, the coal will fracture and break off near the faces. Farther into the pillar, the strength of the pillar increases as the material is under increased confinement and the pillar develops a high-strength core.

The distribution of stress through a pillar is described as a function of the pillar geometry by Karabin and Evanto (1994) with the following equations:

$$S_p(i) = S_1(0.78 + 1.74\frac{x}{h}) \quad \text{(EQ 3.2)}$$

$$e_p(i) = \frac{S_p(i)}{E} \quad \text{(EQ 3.3)}$$

$$S_{R1}(i) = (0.1385 * \ln(x) + 0.413)S_p(i) \quad \text{(EQ 3.4)}$$

$$e_{R1}(i) = 2 * e_p(i) \quad \text{(EQ 3.5)}$$

$$S_{R2}(i) = (0.2254 * \ln(x)) * S_p(i) \quad \text{(EQ 3.6)}$$

$$e_{R2}(i) = 4 * e_p(i) \quad \text{(EQ 3.7)}$$

where $S_p(i)$ is the peak strength of the i-th element, S_1 is the in-situ coal strength, x is the distance of the element center from the pillar edge, h is the height of the coal seam, $e_p(i)$ is the peak strain of the i-th element, E is the Young's modulus of the coal seam, $S_{R1}(i)$ is the first residual stress of the i-th element, $e_{R1}(i)$ is the first residual strain of the i-th element, $S_{R2}(i)$ is the second residual stress of the i-th element, and $e_{R2}(i)$ is the second residual strain of the i-th element.

In order to determine the appropriate softening values for the coal seam in the TMM model, a test model of a 14 m × 14 m × 2.7 m coal pillar (3125 zones) was assigned a strength distribution according to Equations 3.2–3.7 and compressed. The stress-strain curve of the test pillar is shown in Figure 3.4. The input parameters for the strength distribution were selected such that the peak strength of the pillar matched the

measured strength of the coal in the Hiawatha coal seam, or 28.5 MPa. As described in Karabin and Evanto (1994), the pillar behaves elastically up to its peak strength, drops to a first residual value, and gradually decreases to the second residual value, where the stress levels off. In this instance, the residual strength is 16.0 MPa, or approximately 56% of the intact strength. The softening behavior seen in Figure 3.4 is applied in the model by linearly reducing the cohesion after failure to a residual value that is approximately 56% of the intact cohesion at a strain of 0.045. As with the rock layers, if a zone in the coal seam fails in tension, it is reduced to zero tensile strength.

3.2.3. Gob

One of the most important aspects of modeling a longwall mine is representation of the caving behavior. In this model, the caving behavior is simulated according to Singh and Kendorski (1981) and Pappas and Mark (1993). The behavior is represented by varying the modulus of gob material as it caves and is recompacted. Additionally, interfaces are placed between major stratigraphic layers in the roof to allow them to separate.

When the roof of a mine fails, it caves and falls into the void created by mining activity. When this occurs, the rock weakens and the modulus of the failed material drops, causing stress to shed away from the failed area and into the surrounding rock mass. Later in the caving process, overlying material will also fail or bend and load the previously failed gob material, recompacting it and causing it to stiffen, which is represented by an increase in the elastic modulus. The following equation from Salamon (1990) describes the stress-strain relation for backfill material or aggregates:

$$\sigma = \frac{E_0 \varepsilon}{1 - \varepsilon/\varepsilon_m} \quad \text{(EQ 3.8)}$$

where σ is the vertical stress (compression is positive), E_0 is the uncompacted Young's modulus, ε is the strain, and ε_m is the strain at infinite pressure. Pappas and Mark (1993) derived an expression for the tangent modulus of an aggregate material by taking the derivative of Equation 3.8 with respect to the strain. This yields the following equation:

$$E_t = E_0 + \frac{2\sigma}{\varepsilon_m} + \frac{\sigma^2}{\varepsilon_m^2 E_0} \quad \text{(EQ 3.9)}$$

where E_t is the tangent modulus of the gob material, E_0 is the elastic modulus of the uncompacted caved material, σ is the vertical stress (compression is positive), and ε_m is the strain at infinite pressure.

The changing modulus of the gob material as it is recompacted is represented with a routine defined using *FLAC*^{3D}'s built-in programming language, FISH. When a zone in the roof fails in tension and falls into the opening created by mining, the elastic modulus of the zone is reduced to a residual value. The modulus of the zone is then varied using Equation 3.9 as the zone is gradually reloaded by the overlying zones.

The appropriate values for the uncompacted gob modulus and strain at infinite pressure were selected to be comparable to literature values and produce subsidence that matches the subsidence measured at the mine. The values for gob modulus reported in literature cover a wide range between 7 MPa and 2,000 MPa (Mohamed 2003). The uncompacted modulus was initially selected as 250 MPa, which was the value used by Pierce and Board (2010) for their longwall modeling environment. The uncompacted modulus was increased to 500 MPa, which is still well within the reported range of gob

moduli, to better match the mine's subsidence data. The strain at infinite pressure was set to 0.423, which is the average of the values in Pappas and Mark (1993). The gob modulus is relatively insensitive to the value selected for the strain at infinite pressure because the uncompacted modulus is several times larger than the stresses developed in the failed gob zones.

In addition to recompaction of the gob, interfaces were placed between the stratigraphic layers in the roof to allow for bending and separation between the layers. The interfaces obey the Mohr-Coulomb failure criterion and are assigned a friction angle of 30° and cohesion of zero. The only movement expected along the interfaces is separation or slip; as a result, the stiffnesses assigned to the interfaces can be set to large values according to the equation provided by Itasca (2013b).

3.3. Material Properties

Material properties for the roof and floor strata are based on properties presented in Jones (1994). The compressive strength for the coal seam was taken from a coal pillar strength study conducted by Pariseau et al. (1977). The properties for the intact rock and coal are listed in Table 3.1. The friction angle and cohesion were determined from the unconfined compressive strength and the tensile strength using the following relations:

$$\sin\phi = \frac{C_0 - T_0}{C_0 + T_0} \qquad \text{(EQ 3.10)}$$

$$c = \frac{\sqrt{C_0 T_0}}{2} \qquad \text{(EQ 3.11)}$$

where ϕ is the friction angle, C_0 is the unconfined compressive strength, T_0 is the tensile strength, and c is the cohesion.

Material properties testing was conducted on core from a single drill hole located on the Trail Mountain property after the modeling work was completed. The samples that were tested were from the Blackhawk Formation and Star Point Sandstone. The densities of the formations were within 3% of the values used in the model, while the tensile strengths were approximately double the values used in the model. The difference between the lab strengths and the strengths used in the model are reasonable because the samples were dry and only the units that were competent enough to be cut into samples were included in the testing. The difference in properties would result in changes in stresses and displacements of less than 10%.

3.3.1. Joints

The strata at the TMM have moderately developed joints with two near-vertical joint sets, one striking N10°E and one striking N75°W (Jones 1994). There is also a near-horizontal bedding plane. The presence of jointing in the rock mass must be accounted for in a numerical model. Jointing can significantly impact the strength of and cause anisotropy in a rock mass. Jointing also influences the amount and direction of caving in a caving mine (Sainsbury 2012). There are two ways of representing joints in a numerical model: explicitly with a discontinuum method and implicitly with an equivalent continuum. In a discontinuum method, such as the discrete element method, the rock mass is modeled as intact blocks of rock separated by discontinuities or joints that are assigned their own strength properties. Explicitly representing joints is considered to be the most realistic method for representing joints because it allows for the

simulation of large displacements and rotations that may occur along the discontinuities (Kulatilake et al. 2013). Explicitly representing joints can be very computationally intensive because of the large number of joints that must be represented (Kulatilake et al. 2013).

While an explicit method is a more realistic method of representing joints, it is possible to obtain reasonable behavior using a scheme that implicitly represents joints with careful selection of input parameters (Wang et al. 2012). In an implicit or equivalent continuum method, jointing in the rock mass is represented by adjusting the material properties of the rock mass such that it behaves as though the joints are present. Equivalent continuum methods are more common because they are less computationally intensive and easier to implement.

A variety of methods have been used to represent an equivalent continuum. One such method is to simply reduce material properties by a set percentage to mimic the behavior of the jointed rock mass (Wang et al. 2012). Another method treats the joints and intact rocks as separate materials in a composite and calculates the properties for that composite, as in the method outlined by Pariseau (2012). The method used by the Itasca Consulting Group to represent joints is a constitutive model known as the Ubiquitous-Joint constitutive model and its variation, the SUBI constitutive model (Itasca 2013c). This constitutive model represents a single weakness plane at a user-specified orientation in each zone of the model. The strengths and failure criterion of the intact rock and the joint are treated separately. *FLAC*^{3D} first checks for failure of the intact rock and applies a plastic correction to the stress, if necessary. *FLAC*^{3D} then checks for failure of the

weakness plane and applies a plastic correction to the stress corresponding to the joint failure.

One flaw of the Ubiquitous-Joint/SUBI constitutive models is that they use a nonphysical method of adjusting stresses to account for joint failure. The stress of the entire zone is adjusted to equal the failure envelope of the weakness plane if failure is detected in the orientation of the weakness plane. As a result, the stress in the zone may be biased by the joint, causing the stress to be lower than what would be observed in the rock mass. This effect becomes more pronounced as zone size increases.

Joints are specified in the TMM model by building a discrete fracture network (DFN). A DFN is a set of statistical distributions describing the geometrical characteristics of a set of joints. $FLAC^{3D}$ generates a set of disk-shaped fractures that obeys the DFN until some stopping criteria relating to the density of fractures is met. In the TMM model, the P32 density was used as the stopping criteria for the DFN. The P32 density is the total fracture surface area per unit volume and is related to the persistence and spacing of a joint set as follows:

$$P32 = \frac{Persistence}{Spacing} \qquad \text{(EQ 3.12)}$$

Table 3.2 lists the geometrical properties of the three joint sets. The orientations of the joints sets are assumed to follow uniform distributions with minimum and maximum values within ±5° of the reported orientations. The trace lengths are also assigned a uniform distribution. The measured trace lengths for the area vary from 6.09 m to 76.2 m (Jones 1994; Maleki 2005). The strengths and elastic moduli of the joints are assumed to be 1% of the intact rock properties. As with the intact rock, the joints

soften after failure. Either the cohesion or tension are set to zero depending on whether the joint fails in shear or tension. The joint friction angles were assigned to be 30°.

The elastic moduli of the joints are not accounted for in *FLAC*^{3D}, so an equivalent Young's modulus and shear modulus were calculated for each zone depending on the joint set that is applied to the zone. The SUBI model assumes isotropy, so the equivalent moduli in the vertical direction were assumed to apply to the entire zone, which may not be an accurate assumption. The joints dip either near-vertically or near-horizontally (parallel or perpendicular to the loading direction); therefore, simple relationships could be used to calculate the equivalent moduli (Pariseau 2012). The following equation describes the equivalent Young's modulus for vertically-dipping joints, which are parallel to the loading direction:

$$E_{eq} = f_r E_r + f_j E_j \qquad \text{(EQ 3.13)}$$

where E_{eq} is the equivalent Young's modulus, f_r is the fraction of the zone that is made up of intact rock, E_r is the Young's modulus of the intact rock, f_j is the fraction of the zone made up of joints, and E_j is the Young's modulus of the joints. In order to determine the fraction of the zone that is made up of joint, a joint thickness of 2.54 mm was assumed. For horizontally-dipping joints, or joints that are perpendicular to the loading direction, the equivalent Young's modulus may be calculated as follows:

$$\frac{1}{E_{eq}} = \frac{1}{E_r} + \frac{1}{SE_j} \qquad \text{(EQ 3.14)}$$

where E_r is the equivalent modulus of the rock, E_j is the equivalent modulus of the joints, and S is the joint spacing. The joint thickness is neglected in this equation. Similar equations describe the equivalent shear modulus.

After the DFN has been generated and joint properties have been assigned, the joints are embedded in the model using the SUBI constitutive model. The joint properties that are assigned to each zone in the model are selected based on which joints from the DFN intersect the zone. One limitation of the Ubiquitous-Joint and SUBI constitutive models is that they only account for one plane of weakness per zone. When multiple joint sets intersect a particular zone, *FLAC*^{3D} determines which joint is represented in the zone based on a user-specified dominance, where the lowest dominance corresponds to the joint that has the highest priority. If only a small portion of a lower dominance fracture intersects a zone, the entire zone will take on the properties of this fracture, even though the fracture should only have a small influence on the zone. Consequently, the joint set with the lowest dominance may exert an excessive influence on the model results. Due to the coarse grid size of the TMM model, this effect is even more pronounced because the zone sizes are larger than the joint spacings, causing the lowest dominance joint to be present in nearly every zone.

In the model, the horizontal bedding plane is given the lowest dominance, which is necessary to induce caving. The next lowest dominance is the N10°E joint set, which is the primary joint set in the Cottonwood Tract (Maleki 2005), followed by the N75°W joint set. Joints are applied to all layers in the model except the Mancos Shale. Additionally, the bedding plane is not included in the Hiawatha Coal Seam.

3.4. Boundary Conditions

The boundary conditions for the model consist of roller boundaries on the bottom and sides of the model. The boundary conditions are applied by fixing the displacements in the direction perpendicular to the side of the model that is constrained. The top of the model is allowed to remain free.

In order to prevent the overlap of roof and floor zones in the mined-out area, an interface was applied to the zones in the immediate roof. As with the interfaces between the roof strata, the interface on the roof zones has a friction angle of 30°, cohesion of zero, and large stiffness.

3.5. Initial Stress State

The initial stress state is determined in two parts, one to account for the "tectonic stresses" and one to account for "induced stresses". According to Zoback et al. (1989), tectonic stresses are made up of the stresses from large-scale, regional forces, while the induced stresses are those stresses from local effects such as topography, anisotropy, and effects of erosion. In the tectonic part of the initial stress determination, loading is assumed to be caused by gravity alone. The model initially consists of a series of horizontal layers, seen in Figure 3.1a. The vertical stress is assumed to be the maximum compressive stress and is due to the weight of the rock calculated by:

$$\sigma_v = \rho g h \qquad \text{(EQ 3.15)}$$

where σ_v is the vertical stress, ρ is the density of the material, g is the gravity constant (9.81 m/s^2), and h is the depth to a given point in the model. The horizontal stresses are equal and are a fraction of the vertical stress, given by:

$$\sigma_h = \left(\frac{\nu}{1-\nu}\right)\sigma_v \qquad \text{(EQ 3.16)}$$

where σ_h is the horizontal stress, ν is Poisson's ratio, and σ_v is the vertical stress. The average Poisson's ratio of the layers was used. Gravity was applied and the model was then stepped to equilibrium to adjust the stresses according to the differing material properties in each layer.

The second part of the initial stress state is the determination of induced changes due to erosion and the topography. The effects of topography were accounted for in the model by removing the material above the topographic surface and stepping to equilibrium (Figure 3.1b). The assumption behind the topography excavation is that the current topography was reached primarily through erosion of the strata, which is valid in the region included in the model, and not by tectonic activity.

3.6. Excavation Sequence

The mine workings are excavated in several stages, shown in Figure 3.3. First, Panels 5–11 are excavated sequentially and the model stepped to equilibrium to provide the initial stress state for Panels 12 and 13. Next, the mined portion of Panel 12 is excavated one row of zones at a time (14-m increments) and the model is stepped to equilibrium after each row. Panel 13 is divided into five pieces, with each piece representing the monthly production of the panel. As with Panel 12, the five pieces of Panel 13 are also excavated one row of zones at a time and the model is stepped to equilibrium after each row. Excavation of the workings is conducted by changing the

mechanical model of their zones to null, causing *FLAC*^{3D} to ignore them in future calculations.

3.7. Unbalanced Force Ratio

A major problem with a large numerical model is its associated runtime. When conducting a mine-wide analysis, it is possible for a single trial to take several days depending on the computer and the setup of the model. In order to maintain a practical runtime for the TMM model, adjustments were made to the unbalanced force ratio used to determine equilibrium. The unbalanced force ratio is the ratio of the average unbalanced force at all gridpoints in the model to the average applied force at all gridpoints in the model. By default, *FLAC*^{3D} stops cycling when the unbalanced force ratio reaches 1E-5, which provides high precision results but results in a large runtime. A larger unbalanced force ratio can be used to reduce the runtime, but there is a tradeoff between the runtime and the precision in the model that must be considered.

In order to determine the best value for the unbalanced force ratio, a small test model was built and several trials were conducted with unbalanced force ratios ranging from 1E-5 to 1E-3. The test model features an excavation that is 648 m long by 252 m wide (46 × 18 zones) and consists of approximately 392,000 zones. On an HP Z800 with two Intel Xeon X5687 processors, the runtimes for the model range from 24 to 212 minutes. Figure 3.5 shows a plot comparing the runtime of the test model and the associated errors for the average vertical stress, seam level displacements, and surface subsidence relative to an unbalanced force ratio of 1E-5. As the unbalanced force ratio increases, the runtime decreases and the relative errors rapidly increase, reaching as much as 90% for an unbalanced force ratio of 1E-3. From the results of this comparison, it was

determined that an unbalanced force ratio of 1E-4 is a sufficient ratio for this model. The ratio provides a significant reduction in runtime, 75 minutes compared to 212 minutes for the unbalanced force ratio of 1E-5, and increases the error relative to the ratio of 1E-5 by 0.7% for stresses and by 7.8% and 6.4% for seam level displacements and surface subsidence, respectively.

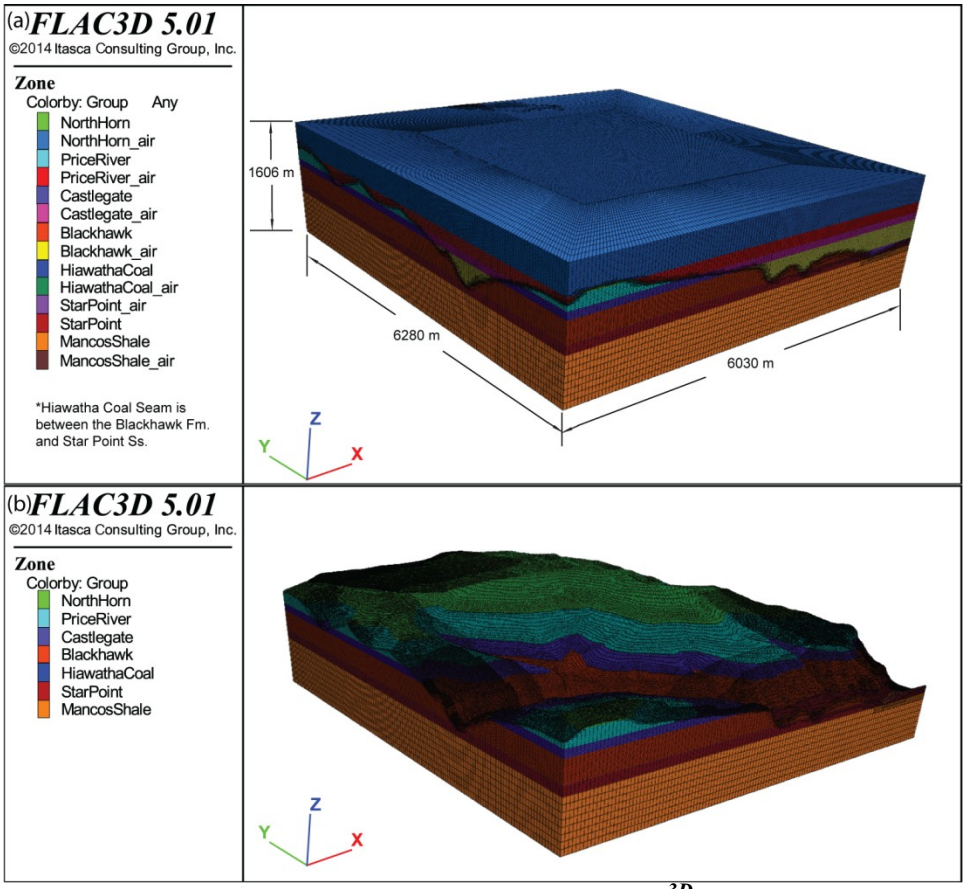

FIGURE 3.1 Grid for the Trail Mountain Mine *FLAC*^{3D} model. Upper image shows all layers of the grid. Lower image shows only layers below the topographic surface.

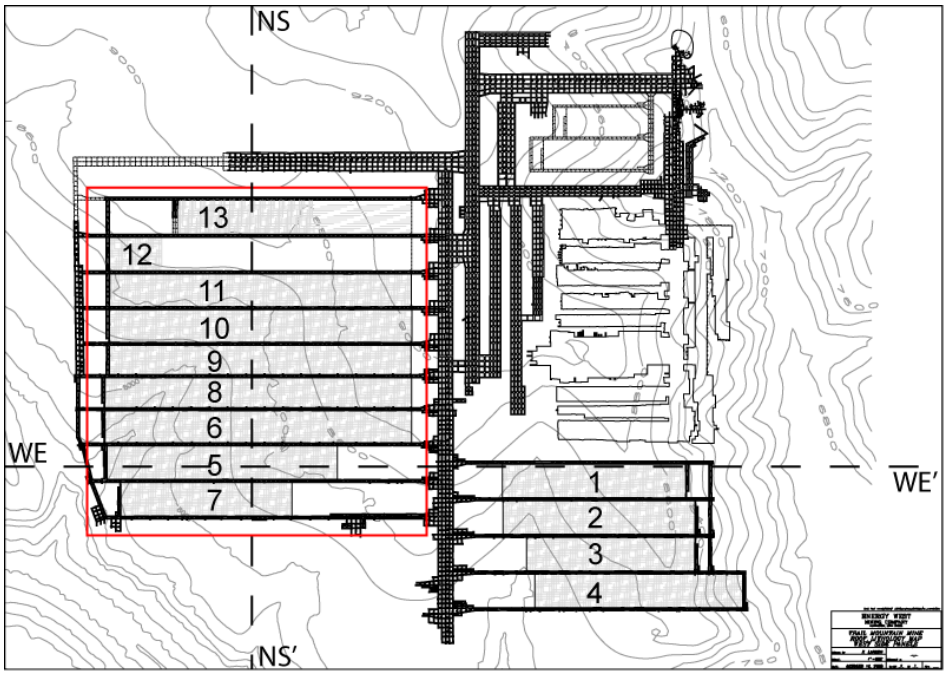

FIGURE 3.2 Map of the Trail Mountain Mine. Hatched areas denote mined-out regions. Numbers denote the extraction sequence of the panels. Thick dashed lines denote locations of subsidence profiles. Red rectangle outlines the panels included in the model. Gray lines show topography.

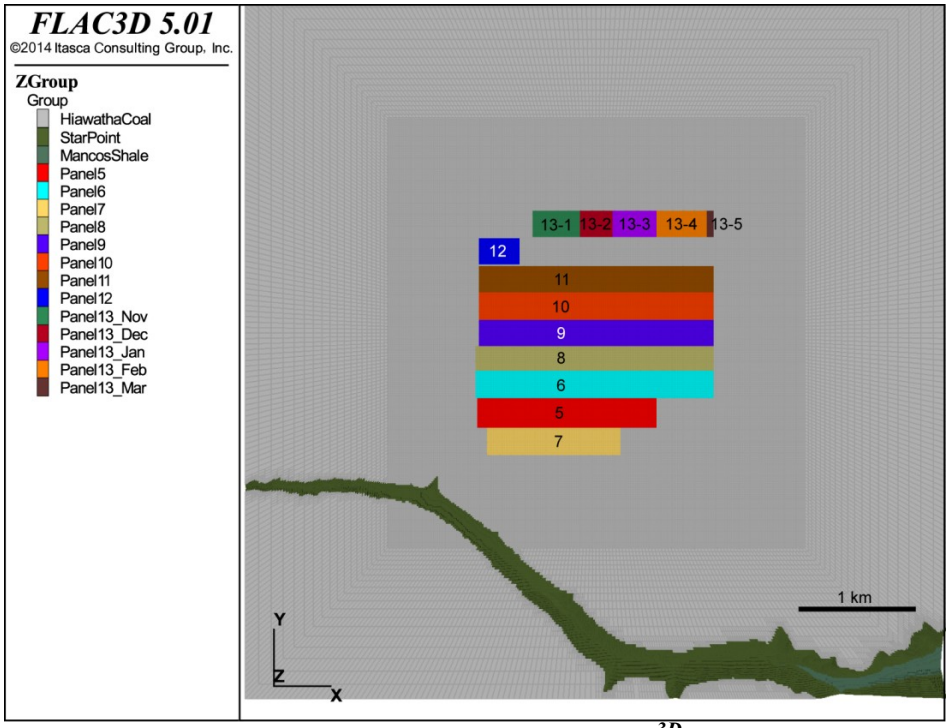

FIGURE 3.3 Mine geometry represented in the *FLAC*^{3D} model

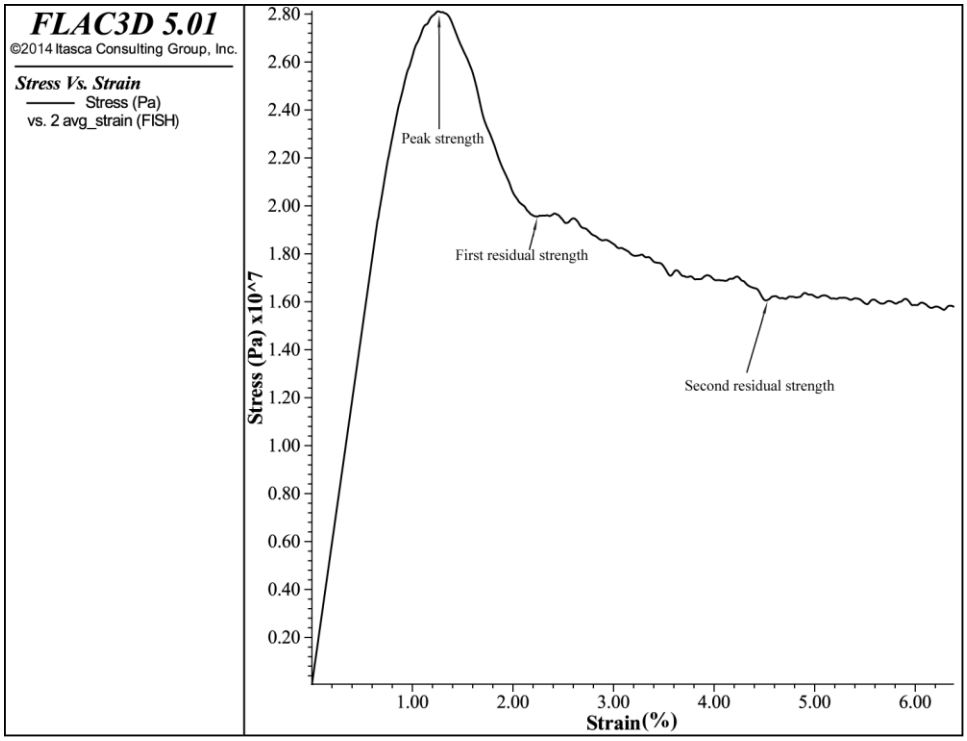

FIGURE 3.4 Stress vs. strain plot for a 14 m × 14 m × 2.7 m coal pillar with a strength distribution derived from Karabin and Evanto (1994)

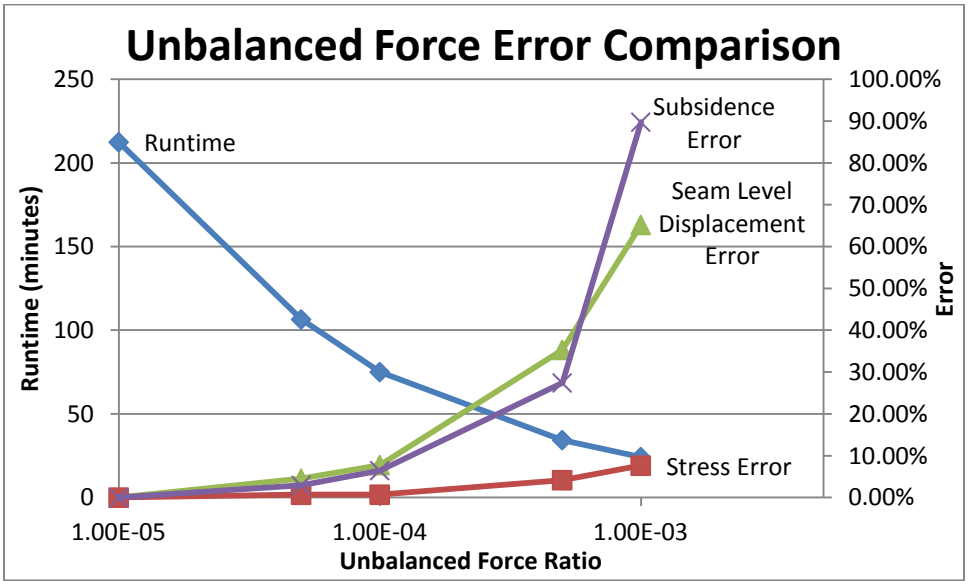

FIGURE 3.5 Comparison of errors for stresses and displacements for different unbalanced force ratios

TABLE 3.1 Intact Rock Properties

Strata	Density, kg/m^3	Young's Modulus, GPa	Shear Modulus, GPa	Unconfined Compressive Strength, MPa	Tensile Strength, MPa
North Horn Fm.	2452.9	17.9	7.10	81.4	4.83
Price River Fm.	2291.7	22.1	8.77	68.8	2.62
Castlegate Ss.	2243.6	20.7	8.48	66.1	2.96
Blackhawk Fm.	2484.0	27.6	11.0	108.0	4.96
Hiawatha Coal	1250.0	2.96	1.32	28.5	1.93
Star Point Ss.	2163.5	17.9	7.34	66.4	2.48
Mancos Shale	2323.7	15.2	5.63	-	-

TABLE 3.2 Joint Orientation and Spacing

Joint Set	Dip	Strike	Spacing, m	Maximum Trace, m	Persistence
Set 1	90°	N10°E	9.14	76.2	0.6
Set 2	90°	N75°W	6.10	76.2	0.6
Set 3	0°	-	7.62	76.2	0.6

4. SINGLE PANEL TEST MODEL

Prior to modeling the west block of panels at the TMM, a model consisting of a single longwall panel was used to verify the behavior of the model as well as to estimate the error associated with the model. Panel 5 was used as the test panel. This panel was the first of Panels 5–13 to be extracted, and was the least affected by older mine workings. Panel 5 was also the only panel from the western block of panels to be mined in 1997, so subsidence reported in that area that year was only due to Panel 5. Four aspects of the model were evaluated in this test: the propagation of stresses through the model, the stress concentrations around the panel, displacements at seam level, and the subsidence developed over the panel.

4.1. Stress Propagation During Initial Stress State Calculation

Stresses were checked in the coal seam and at the bottom of the model before the topography was excavated to ensure that the model behaves continuously and stresses propagate correctly through the model. The stresses were calculated analytically using Equation 3.15 and Equation 3.16. Table 4.1 compares the analytical stresses with the $FLAC^{3D}$ stresses. The error at this stage of the model is acceptable and likely due to an increased unbalanced force ratio of 1E-4 and numerical error.

4.2. Stress Concentrations Around the Test Panel

The stresses at seam level after mining were checked to ensure that the stress concentrations around the longwall panel are reasonable. This test was repeated twice: once using just elastic behavior and once using the full constitutive behavior described in Chapter 3. The stresses in the coal seam after mining were evaluated using the tributary area formula. The tributary area formula assumes that the stress in the coal seam after excavation is based on the proportion of material that is removed and is given by:

$$S_p = \frac{S_v}{1 - R} \qquad \text{(EQ 4.1)}$$

where S_p is the stress in the coal seam, S_v is the vertical stress in the coal seam before mining, and R is the extraction ratio, or the area of the mined-out region over the total area (Pariseau 2007).

The total area used for the extraction ratio is the area of a region that extended approximately 200 m beyond the longwall panel, or a region that is 1,932 m by 630 m. The longwall panel is 1,540 m by 224 m, resulting in an extraction ratio of 0.283. The initial vertical stress in the coal seam is the stress after the topography is excavated. The initial stress was averaged over the region of interest from the model with elastic behavior and determined to be 11.3 MPa. The results of this test are also presented in Table 4.1. The error from the elastic model is fairly small and indicates that stresses are concentrating correctly around the panel.

The error from the trial with the full constitutive behavior is much larger. The large error from the model with the full constitutive behavior can be partially attributed to a combination of the large grid spacing and the way that *FLAC*^{3D} handles joints. As

described in Section 3.3.1, when a joint is assigned to a zone, the zone is assigned the strength properties of the joint, but loses the joint dimension. If the joint fails, the stress of the entire zone is changed, causing the stress to be heavily biased by the joint, especially if the zone is much larger than the joint.

4.3. Seam Level Displacements

The displacements at seam level were checked to make sure that the interface between the roof and floor of the test panel prevented them from overlapping. Figure 4.1 shows a plot of the displacement profiles across the panel and their corresponding seam closure. The roof sag is greater than the floor heave near the gateroads and the floor heave is slightly greater over the center of the panels. At all points, the seam closure is less than or equal to the mining height and there are no areas where either the roof sag or floor heave are excessive. Therefore, this closure check indicates that the interface is effective in limiting displacements.

4.4. Calibration to Subsidence Data

In order to verify that the results of the model reproduce observations from the mine, subsidence developed over the workings in the model was compared with subsidence data reported by the mine.

4.4.1. Subsidence Data for the Trail Mountain Mine

Reports containing subsidence data for the TMM were provided by Energy West Mining for each year between 1996 and 2002. The data consist of descriptions of the areas that were mined during the year covered by the reports, contour maps of the subsidence as determined by aerial survey, and subsidence profiles from west to east and

north to south over both the west and southeast panel blocks. The data of interest are the information for the west panel block for the years 1997 and 2001, which encompass the first year and last year of extraction of the west block of panels. The subsidence profiles were compared with those determined in *FLAC*^{3D}.

4.4.2. Variance Reduction

The fits between the subsidence profiles recorded at the mine and the profiles from *FLAC*^{3D} were evaluated using the variance reduction. The variance reduction is a measure of the difference between the magnitude of observed and predicted data normalized to the magnitude of the observed data (Cohee and Beroza 1994). In this instance, the data are the amount of subsidence at a given location. The variance reduction can be determined using the following equation:

$$VarRed = 100 * \left(1 - \frac{\sum(obs - pred)^2}{\sum obs^2}\right) \quad \text{(EQ 4.2)}$$

where $VarRed$ is the variance reduction, obs is the measured magnitude of subsidence at a given point, and $pred$ is the magnitude of subsidence from *FLAC*^{3D} at a given point. The maximum value of the variance reduction is 100 and it decreases to potentially large negative numbers as the quality of the fit decreases. For this study, a variance reduction greater than 75 is considered acceptable.

4.4.3. Subsidence over Panel 5

Panel 5 was selected as the test panel to be used for the subsidence calibration because it is the first and only panel that was mined from the western block of panels in 1997. As a result, the subsidence measured over this panel is minimally influenced by

other mine workings and can be compared to the results of the *FLAC*^{3D} model. Three trials were conducted with different realizations of the DFN to determine the effects that a different joint distribution would have on the subsidence. The maximum difference between the three runs was 0.06 m, or about 14%. The subsidence profiles for the three runs were averaged for comparison with the measured subsidence data.

Figures 4.2 and 4.3 compare the subsidence profiles measured at the mine with the subsidence recorded by the *FLAC*^{3D} model. The variance reduction is calculated over the gray shaded regions. The subsidence at the mine was not measured beyond these regions. The magnitudes of the subsidence are similar between the measured and *FLAC*^{3D} profiles, though the model profile is slightly deeper and is more continuous than the measured data. The widths of the troughs in the *FLAC*^{3D} profiles are wider than the measured data, which may be because the measured data do not include the entire subsidence trough. The trough is slightly offset between the measured and *FLAC*^{3D} north to south profiles. Variance reductions were calculated as 88.2 from west to east and 82.9 from north to south. Both profiles have variance reductions above 75, and are considered to be good fits over the regions where the variance reduction was calculated.

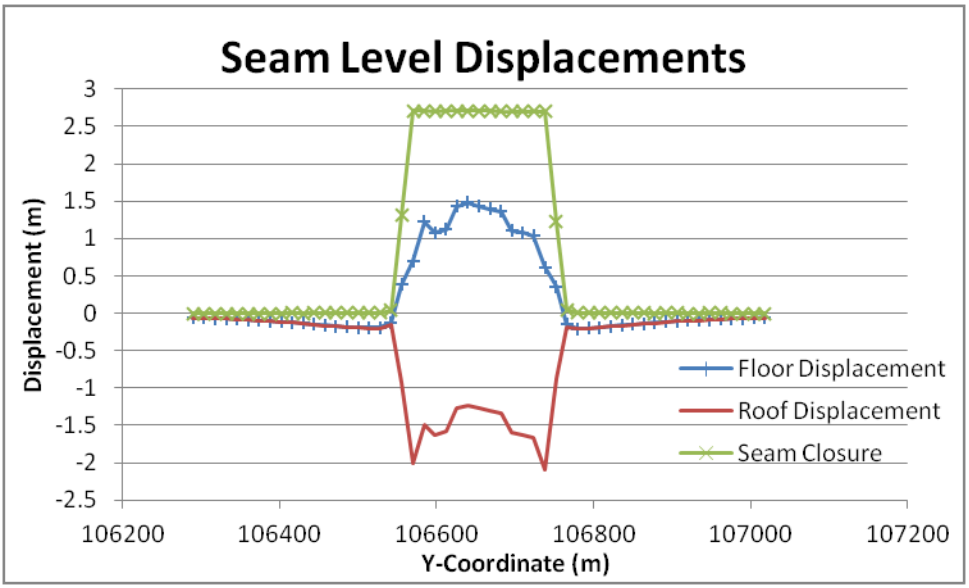

FIGURE 4.1 Displacements for Panel 5 at seam level, looking east

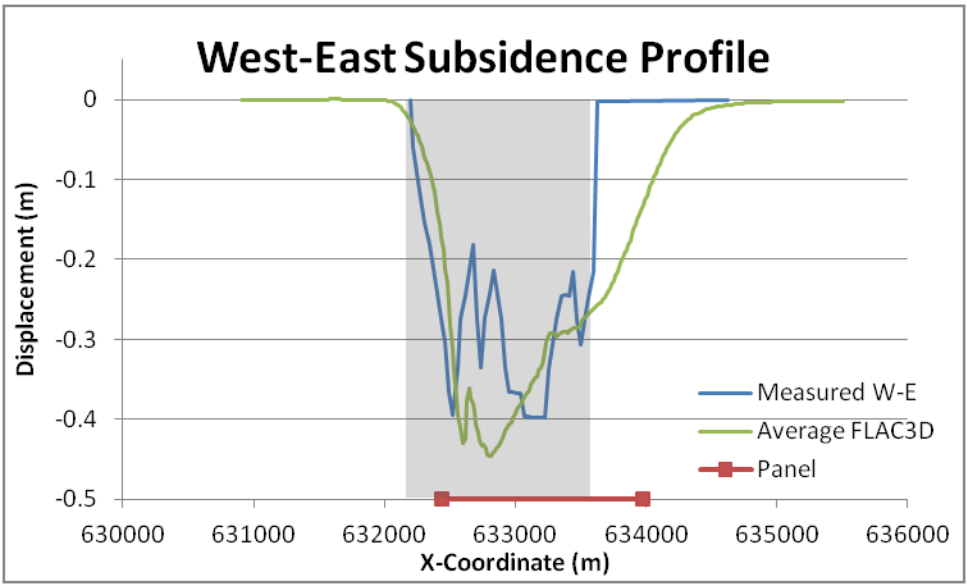

FIGURE 4.2 West to east subsidence profiles from data measured at the mine and recorded in *FLAC*^{3D} after Panel 5 was extracted. Gray shaded region indicates the region over which the variance reduction was computed.

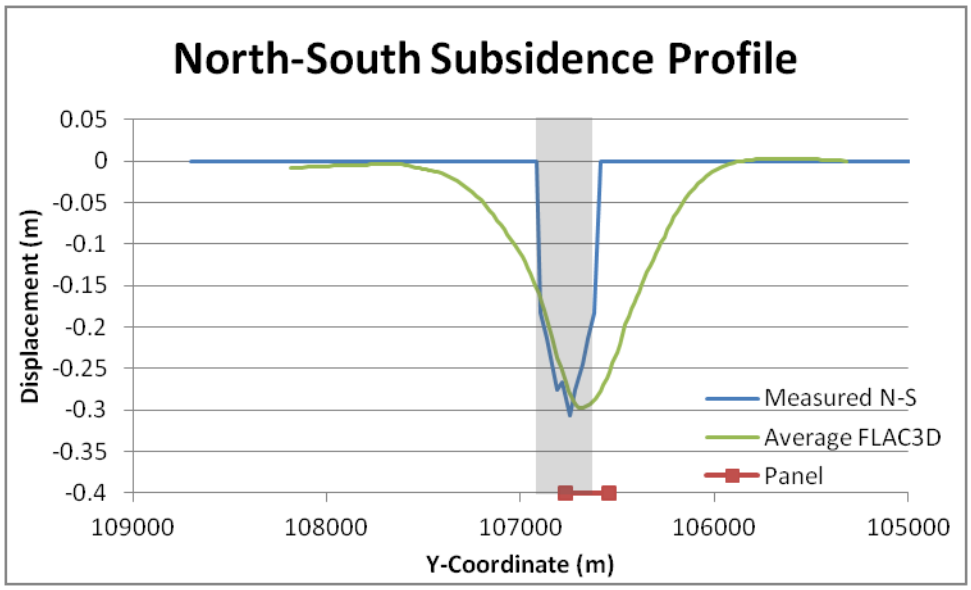

FIGURE 4.3 North to south subsidence profiles from data measured at the mine and recorded in *FLAC*^{3D} after Panel 5 was extracted. Gray shaded region indicates the region over which the variance reduction was computed.

TABLE 4.1 Comparison of Analytical and *FLAC*^{3D} Stresses

Test	Analytical Value, MPa	FLAC^{3D} Value, MPa	Error, %
Vertical Stress, Seam Level	19.3	19.1	1.0
Horizontal Stress, Seam Level	6.11	5.97	2.3
Vertical Stress, Model Base	35.8	34.8	2.9
Horizontal Stress, Model Base	11.3	11.0	2.8
Stress After Excavation, Elastic	15.9	15.3	3.8
Stress After Excavation, Elasto-Plastic	15.9	13.9	12.5

5. MINE-WIDE ANALYSIS RESULTS

The goal of the TMM model is to determine if there are correlations between features of the model, specifically the failed zones and stresses, and the seismicity recorded during the mining of Panel 13 at the TMM. In this chapter, the results of the mine-wide analysis are presented. The subsidence developed in the model is compared with the subsidence recorded at the mine. Zones that failed during the course of mining Panel 13 are identified and compared with the locations and seismic moments of the MIS on Panel 13. Areas of high vertical stress, maximum shear stress, and change in maximum shear stress are identified and compared with the locations of the seismicity.

5.1. Subsidence

As with the test model from Chapter 4, the subsidence from the mine-wide analysis was compared with the subsidence recorded at the mine to ensure that the model reproduces field observations. The subsidence data for the mine from the year 2001 were used in the comparison. Data were provided for the year 2002, but the data are inconsistent in that the subsidence decreases by 0.6 m and the mine reported that the data are suspect. Subsidence profiles are provided for the west-east and north-south directions in Figures 5.1 and 5.2. The locations of the profiles are marked on Figure 3.2. The west to east $FLAC^{3D}$ profile closely matches the data recorded at the mine. The trough reaches the same depth and is approximately the same width as the mine data, though the modeled trough is slightly wider. The north to south profile also extends to a similar

depth as the measured data. The width of the north to south *FLAC*^{3D} trough deviates from the mine data to the north, likely because the subsidence over Panel 13 was not measured because it is separated from the other workings. It is also possible that the subsidence associated with this panel had not fully developed at the time of the survey. The variance reduction was calculated over the gray shaded regions. The variance reduction is 96.7 in the west-east direction and 93.2 in the north-south direction. Both values are well above the cutoff for a good variance reduction.

5.2. Failed Zones

A seismic event occurs when the rock mass fails and radiates energy; therefore, a relationship might be expected between the failed zones in the model and the MIS recorded at the mine. The locations of the failed zones in the *FLAC*^{3D} model were compared with the locations of seismic events to determine if the failures coincide with the seismicity. The seismic moment was also compared with the volume of the failed zones to determine if there is a relationship between the two parameters. If a relationship is found, it could indicate that the energy release from the model could be used as a proxy for potential energy release from seismic events.

Figure 5.3 compares the locations of the failed zones and the locations of the MIS that was recorded in December 2000. The north-south cross-sections in this figure are representative of the failed zones and seismicity along the majority of the panel until reaching the east end, where the seismicity merged across the panel. The failed zones associated with Panel 13 (Figure 5.3a) consist of tensile failures along the bedding planes in the immediate roof and floor of the panel surrounded by shearing of joints that extends approximately 90 m into the roof and 45 m into the floor. The zones around the older

mine workings (Panels 5–11) failed in a similar pattern to those around Panel 13. Additionally, there are zones that have vertical joints that sheared during the initial stress state determination. The seismicity primarily locates on the gateroads of Panel 13 (Figure 5.3b), with the majority of the events locating in the roof within 250 m of mine level.

The failed zones in the model occur in different locations than the seismicity. There are three possible reasons for this difference. First, the model is conducting a static analysis, so the failure mechanisms in the model do not distinguish between failure that happens quickly enough to radiate seismic energy and aseismic failure. The second explanation is related to the failure mechanisms that occur in the model. The failures occurring directly above and below the workings are predominately tensile failures and separations along joints, which are expected to release less energy. Tensile failures are less likely to radiate enough seismic energy to be adequately recorded, which could explain the lack of observed seismicity over the center of the panel (Luo et al., 1990). Finally, there is some uncertainty in the locations of the earthquakes, making it difficult to determine whether failure in a specific zone in the model can be compared to a given seismic event.

The seismic moment, which is a measure of the energy released by the seismicity based on the amount of fault slip, can be estimated from the magnitude of an event using the following empirical equation from Spottiswoode and McGarr (1975):

$$\log M_0 = 17.7 + 1.2M_L \qquad \text{(EQ 5.1)}$$

where M_0 is the seismic moment in N-m and M_L is the Richter magnitude. The TMM coda magnitudes are converted to Richter magnitudes by subtracting 0.44 (Pechmann et al. 2008). In order to accurately compare the seismic moment with the volume of failed zones, only events above a magnitude of completeness of 1.1 were included in the seismic moment calculation.

The volume of the zones that failed around Panel 13 in the model and the seismic moment of events that were recorded during mining of Panel 13 were tabulated on a monthly basis. Figure 5.4 compares how the volume of failed zones and the seismic moment accumulated as the panel progressed. In the *FLAC*^{3D} model, the failures progress at a nearly constant rate as the face advances, resulting in a linear plot for the cumulative failed volume. The cumulative seismic moment also increased as the panel progressed, though at a different rate. As with the volume of failed zones, the seismic moment increases nearly linearly for the first 1060 m of the panel. After this point, the seismic moment increases more rapidly, corresponding to a more rapid increase in the seismicity rate. The volume of failed zones does not show this pattern, indicating that it cannot explain the change in the seismicity rate. This means that the model is either lacking a feature of the mine that could cause the increase in seismicity, or that the failed zones are not related to the seismicity. The absence of a relationship between volume of failed zones and seismic moment is reasonable because there is no spatial relationship between the failed zones and seismicity. Additionally, the failures in the model do not distinguish between zones that would fail seismically or aseismically.

5.3. Vertical Stresses

In addition to examining failures in the model, the stresses in the model were also evaluated. Zones of increased vertical stress were identified to determine if there is a relationship between the stresses and the locations of the seismicity. Figure 5.5 shows the vertical stresses around Panels 12 and 13 at seam level. The stresses around the edges of the panels are higher while the stresses over the panels are lower due to excavation. The area with the greatest vertical stress occurs in the tailgate of Panel 12. Additionally, the vertical stress increases by 13% in the barrier pillar toward the east end of Panel 13, where there was an increase in the seismicity rate. The older mine workings also show an increase in stress toward the east.

Figure 5.6 shows profiles of the vertical stress along the headgate, tailgate, and center of the panel at varying distances from the mine. The presence of jointing in the model resulted in large fluctuations in the stress profiles. In order to more clearly identify trends in the stress, the profiles were smoothed using a moving average with a 100 m window around the point shown on the profile. Within 100 m of the mine, the stresses on the gateroads are similar in magnitude and greater than the stresses on the center of the panel. The stress on the panel center is much lower than the gateroad stresses due to failures in the roof and floor. At 300 m above the workings, the stresses over the gateroads are similar to the panel center, likely because the roof is not failing at this distance. The vertical stress gradually increases on the gateroads as the panel progresses to the east. Additionally, there is a slight dip in stress followed by an increase in stress, with corresponding fluctuations in the topography, after which the seismicity merges across the panel.

From Figure 1.1, the seismicity recorded on Panel 13 primarily clusters along the gateroads before merging into a single large cluster at the end of the panel. Elevated stresses on the gateroads are consistent with seismicity occurring on the gateroads, while the low stress over the center of the panel is consistent with a lack of seismicity. The stresses are highest on the tailgate of Panel 12, which is consistent with the seismicity that caused the panel to be abandoned. An increase in the stress over the center of the east end of the Panel 13 would be expected for a cluster of seismicity over the end of the panel; however, the plots of vertical stress do not show this trend. The plots do show a general increase in vertical stress to the east, coinciding with increasing depth of cover, that may be related to the increase in the number of events. The results presented in this section indicate that there could be a weak correlation between increased vertical stress and the locations of MIS on Panels 12 and 13.

5.4. Maximum Shear Stresses

Areas of high maximum shear stress were also identified and compared to the locations of the MIS. Figure 5.7 shows the maximum shear stress around Panels 12 and 13 at seam level. The stress pattern is very similar to that seen in Figure 5.5 for the vertical stress. The maximum shear stress is higher on the gateroads, particularly the tailgate of Panel 12. As with the vertical stress, the maximum shear stress is lower within the mined-out region as a result of excavation and caving. The maximum shear stress is slightly elevated in the barrier pillar approaching the east end of the panel and the older workings once again show increased stress to the east.

Profiles of the maximum shear stress along the headgate, tailgate, and center of Panel 13 are provided in Figure 5.8. The profiles were measured at seam level, 100 m

above and below the mine, and 300 m above the mine. The shear stress profiles were smoothed using a moving average with a 100 m window around the point shown on the profile to reduce the stress fluctuations caused by jointing. The maximum shear stress is higher in the gateroads relative to the center of the panel within 100 m of mine level. At 300 m above the mine, the stress over the gateroads is comparable to the stress over the center of the panel. The stress is comparable between the headgate and tailgate of the panel; however, there is a region 100 m above the mine where stress on the tailgate is significantly higher than stress on the headgate. At seam level, the stress remains relatively constant along the length of the panel. At other elevations, the gateroad stress tends to increase to the east, which is most noticeable at elevations other than seam level. There is a dip in shear stress followed by a significant increase in stress toward the end of the panel, coinciding with a fluctuation in the topography (Figures 5.9 and 5.10).

Figures 5.9 and 5.10 compare the maximum shear stresses on the gateroads at 100 m into the mine roof with the seismic moment of events that located along the headgate and tailgate of the panel. The seismic moment was calculated in the same manner as in Section 5.2. Only the 365 events above a magnitude of completeness of 1.1 were included. An event was determined to have occurred on the headgate if it was north of the panel center and on the tailgate if it was south of the panel center. The moment fluctuates significantly across the panel because there are few events, making it difficult to identify trends. Additionally, there is some uncertainty in the locations of individual events. To account for this, the seismic moment was smoothed using a moving average with a 100 m window. Overall, the shear stress and seismic moment show good agreement. Areas of the panel that exhibit high shear stress are immediately followed by

areas of increased seismic moment as the shear stress decreases. This suggests that the seismic events accompany the release of energy from the rock mass as it de-stresses. There is a region of increased seismic moment at the very beginning of the panel that does not correspond to an area of high shear stress in the model, which is likely due to the proximity of Panel 13 to Panel 12.

Elevated stresses on the gateroads are consistent with seismicity occurring on the gateroads. The high shear stress on the tailgate of Panel 12 could be related to the excessive seismicity that resulted in Panel 12 being abandoned. As with the vertical stresses, there is not a peak in stress over the center of Panel 13 to indicate that a cluster would form across the end of the panel. There is a trend of increasing stress as the panel progresses east, which peaks about 100 m before the seismicity merges across the panel, supporting the increase in the amount of seismicity at the end of the panel. One interesting feature of the stresses that is observed with both the vertical stress and the maximum shear stress is a decrease followed by a significant increase in stress that coincides with changing topography. The seismicity merges across the panel and the seismicity rate greatly increases 100 m after this point. This pattern suggests that the change in topography may be related to the increase in the seismicity rate. Finally, the region of increased stress on the tailgate between 370 m and 770 m may be related to a slight increase in seismicity on the tailgate compared to the headgate.

5.5. Change in Maximum Shear Stress

A common method in seismology for evaluating whether stresses are more likely to promote or inhibit future seismicity is to calculate the Coulomb failure stress change, given by the following equation:

$$\Delta CFS = \Delta\tau - \mu(\Delta\sigma - \Delta P) \quad \text{(EQ 5.2)}$$

where ΔCFS is the Coulomb failure stress change, $\Delta\tau$ is the change in shear stress along a weakness plane, μ is a frictional coefficient, $\Delta\sigma$ is the change in normal stress along a weakness plane, and ΔP is the change in pore pressure (Stein 1999). The use of Equation 5.2 requires knowledge of the orientation of the plane that slips to generate the future seismicity, but the failure mechanisms and failure planes are largely unknown for the TMM dataset. In order to eliminate the need for the failure plane orientation, the change in maximum shear stress was used as a simplification of this criteria. Seismicity can occur as a result of relatively small stress changes (Stein 1999), so for this study, a stress change of 0.1 MPa is considered significant enough to potentially induce seismicity.

Figure 5.11 shows the evolution of the change in maximum shear stress as Panel 13 is mined. Each frame represents the stress change at seam level caused by the excavation of material during a one-month period. Zones with a positive maximum shear stress change of greater than 0.1 MPa are shaded, while lower and negative-valued areas are shown in white. The stress change pattern for each month's excavation is similar. There are areas of elevated stress changes immediately surrounding the excavation with smaller stress increases extending approximately one panel-width from the excavation. As the panel progresses, there is increased stress in the previously mined-out region, consistent with the recompaction of the gob material as it is loaded by the overburden. There is also a front abutment stress that extends 28–84 m ahead of the face. The shear stress changes from the November excavation show positive stress changes around the mined-out portion of Panel 12 and part of Panel 11 in addition to the stress changes

surrounding the mined-out portion of Panel 13. This indicates that there is some interaction between these workings, which may have influenced the small cluster of seismicity that occurred at the beginning of mining in Panel 13.

The regions of increased shear stress on the gateroads are consistent with seismicity occurring on the gateroads, with stress changes being greater on the tailgate. During the February 2001 excavation, the stresses over the east end of the panel decrease rather than increase, indicating that the seismicity should not merge across the panel, despite the locations of the seismicity recorded at the mine. There are two possible reasons for the cluster not to appear in the model. It is possible that the change in shear stress alone is not a sufficient indicator of the potential for seismicity. Another explanation is that the model does not account for some factors that could cause the cluster. Changes in near-seam geology and the presence of old room-and-pillar workings to the east of Panel 13 that were not included in the model could influence the stresses at the east end of the panel and potentially cause seismicity to occur above the panel.

A cross-section of the maximum shear stress change is provided in Figure 5.12. Areas of high maximum shear stress change occur along the gateroads and the region of increased stress extends greater than one panel-width on either side of the panel, forming nearly symmetrical stress lobes. The increased stress persists 300–350 m into both the roof and floor of the mine. Increased stresses extending into the roof of the mine are consistent with the extent of the seismicity in the roof. The increased stress in the floor indicates that there should be an equal amount of seismicity in the roof and floor, though relatively few events located in the floor (Figure 1.1b). The discrepancy could be partially caused by a mislocation of the event depths; however, the relative error between

events is very small (< 10 m), making it unlikely that the locations could spread enough to extend 300 m into both the roof and floor. It is also possible that the change in maximum shear stress alone is not a sufficient indicator of whether or not seismic events might occur.

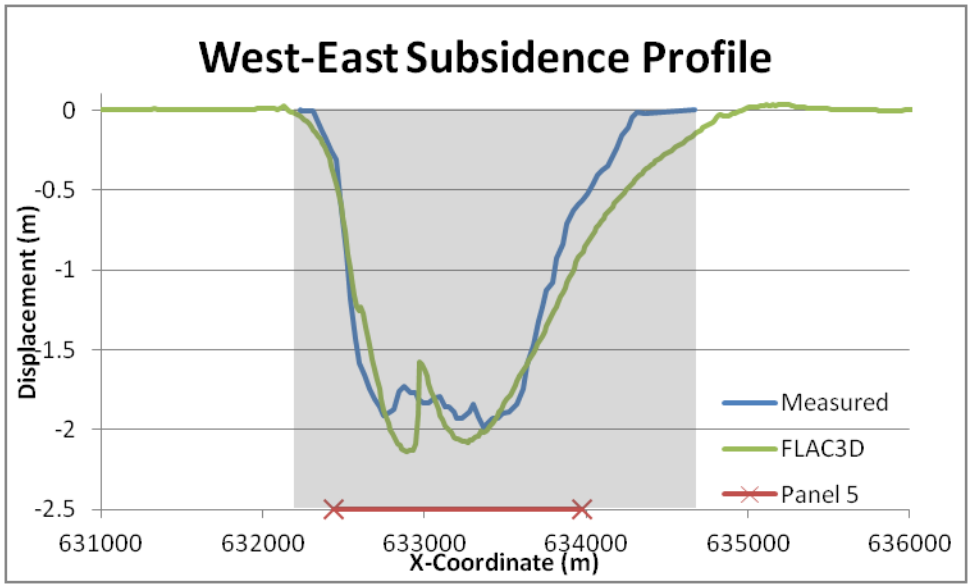

FIGURE 5.1 West to east subsidence profiles from data measured at the mine and recorded in *FLAC*^{3D} after all panels were extracted. Gray shaded region indicates the region over which the variance reduction was computed.

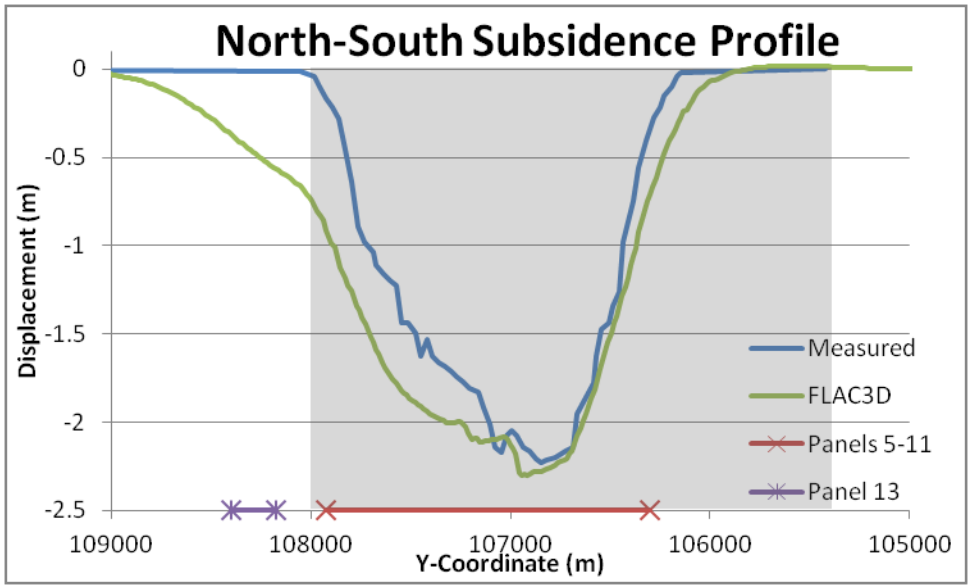

FIGURE 5.2 North to south subsidence profiles from data measured at the mine and recorded in *FLAC*^{3D} after all panels were extracted. Gray shaded region indicates the region over which the variance reduction was computed.

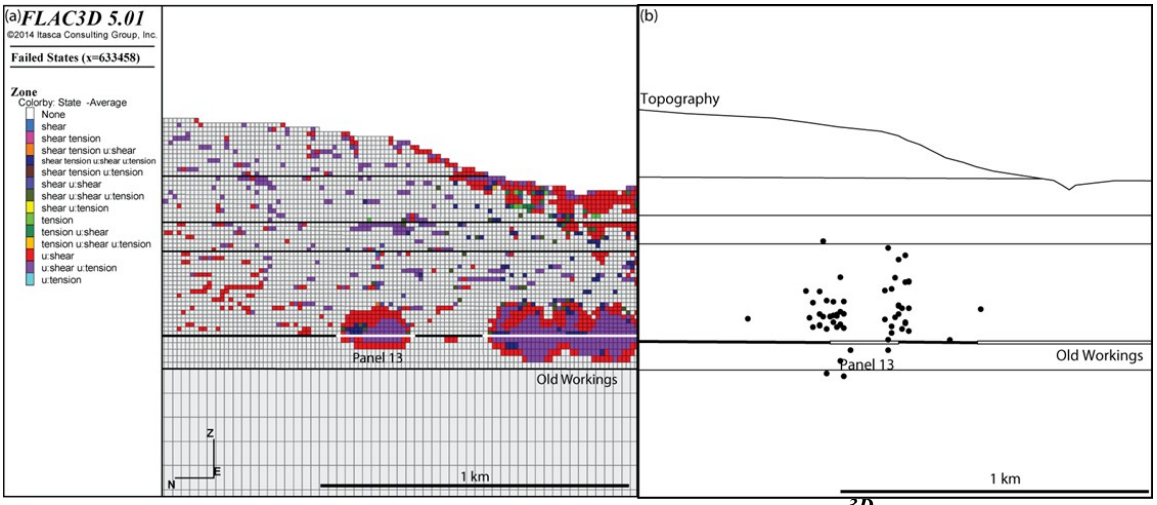

FIGURE 5.3 Comparison of (a) the failed zones in the *FLAC*^{3D} model and (b) locations of seismicity recorded during December 2000 in a north to south cross-section. Black horizontal lines show stratigraphic layering.

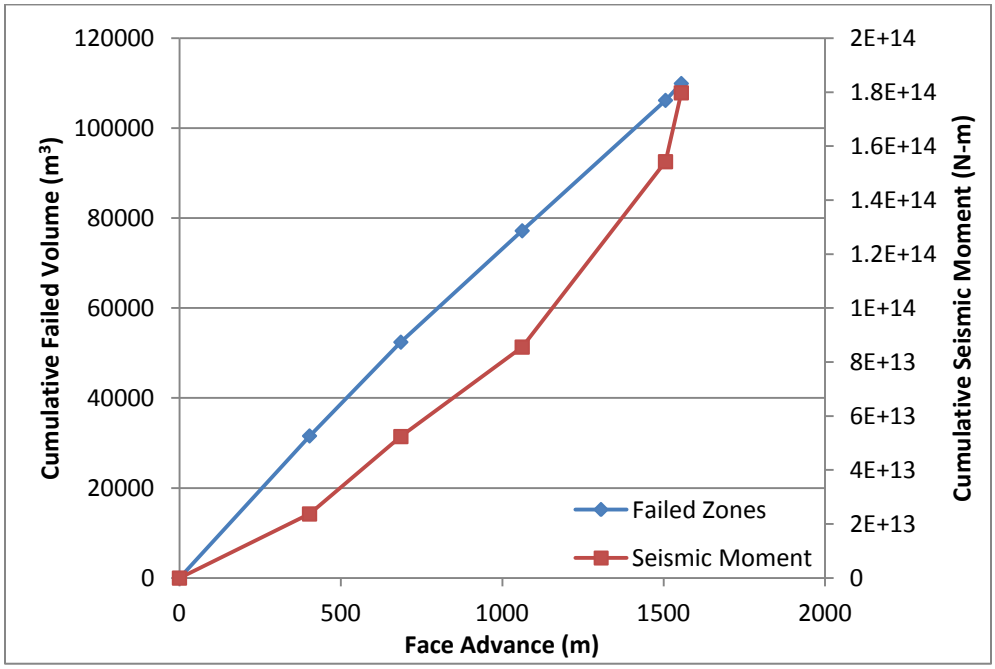

FIGURE 5.4 Comparison of the cumulative volume of zones that failed in the *FLAC*^{3D} model and the cumulative seismic moment of events recorded on Panel 13

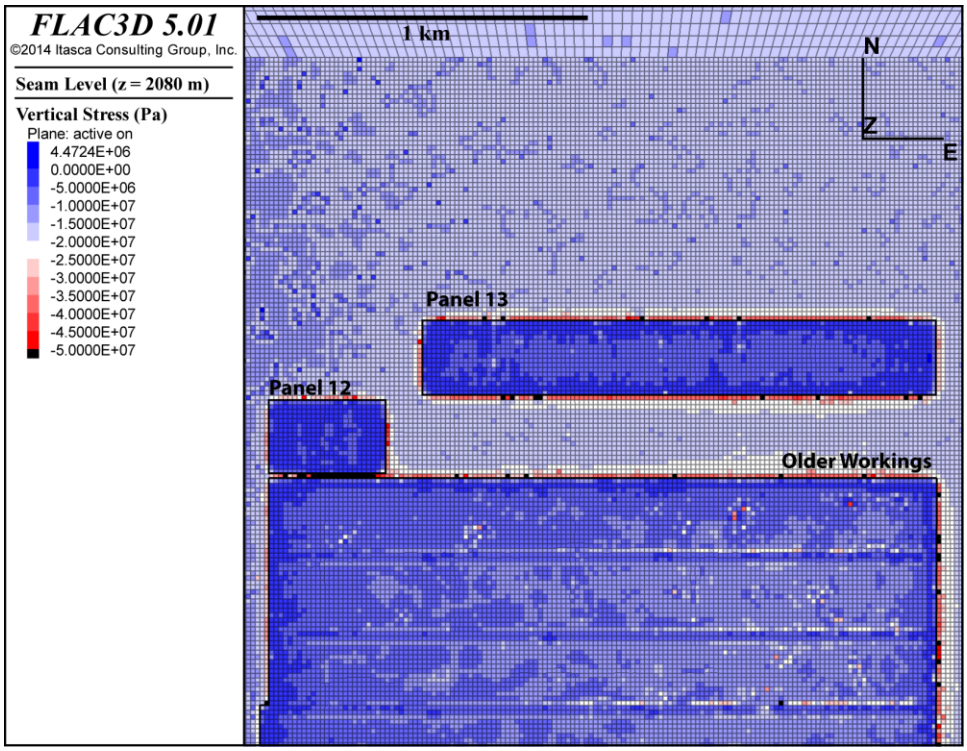

FIGURE 5.5 Plot of vertical stresses around Panels 12 and 13 after all panels were extracted. Plot is at seam level. Compressive stress is negative.

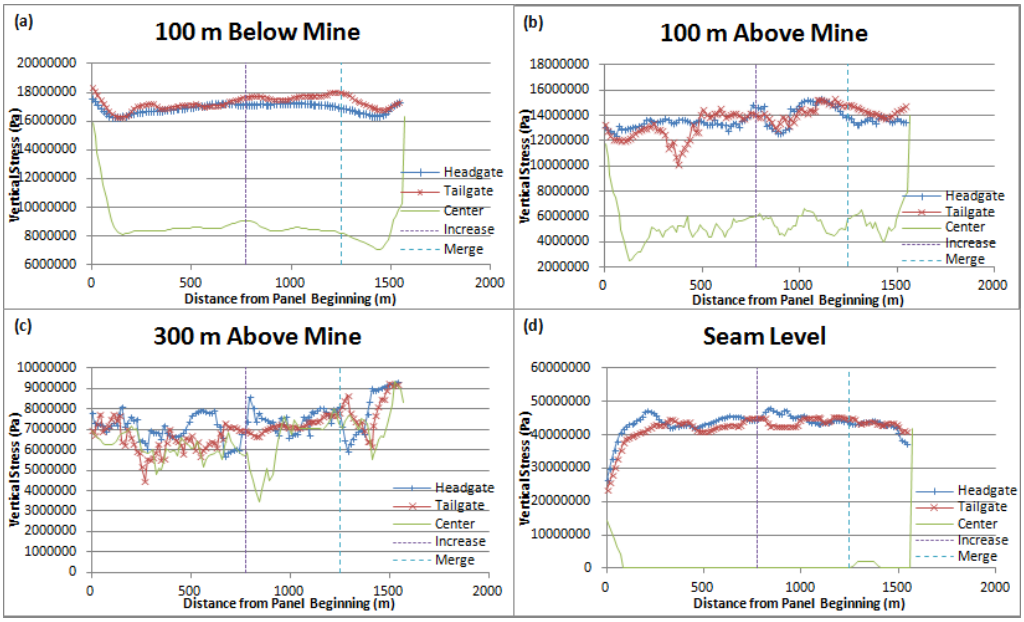

FIGURE 5.6 Vertical stress profiles from west to east on the headgate, tailgate, and center of the panel at (a) 100 m below mine level, (b) 100 m above mine level, (c) 300 m above mine level, and (d) at seam level. Vertical dashed lines indicate where the amount of seismicity increases and merges across the panel.

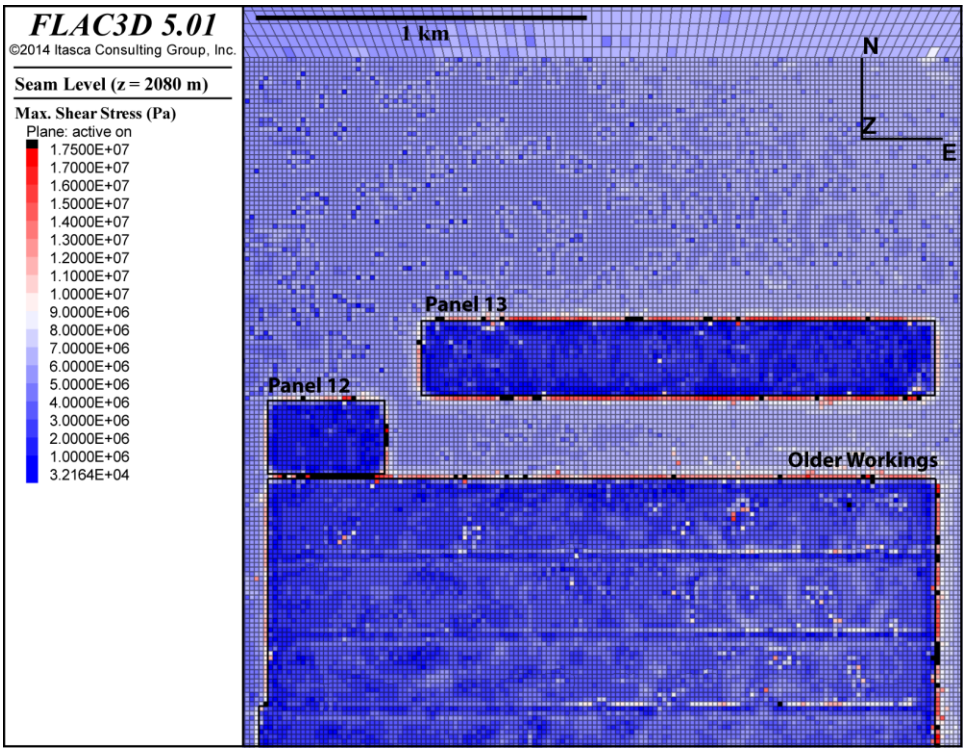

FIGURE 5.7 Plot of maximum shear stresses around Panels 12 and 13 after all panels were extracted. Plot is at seam level.

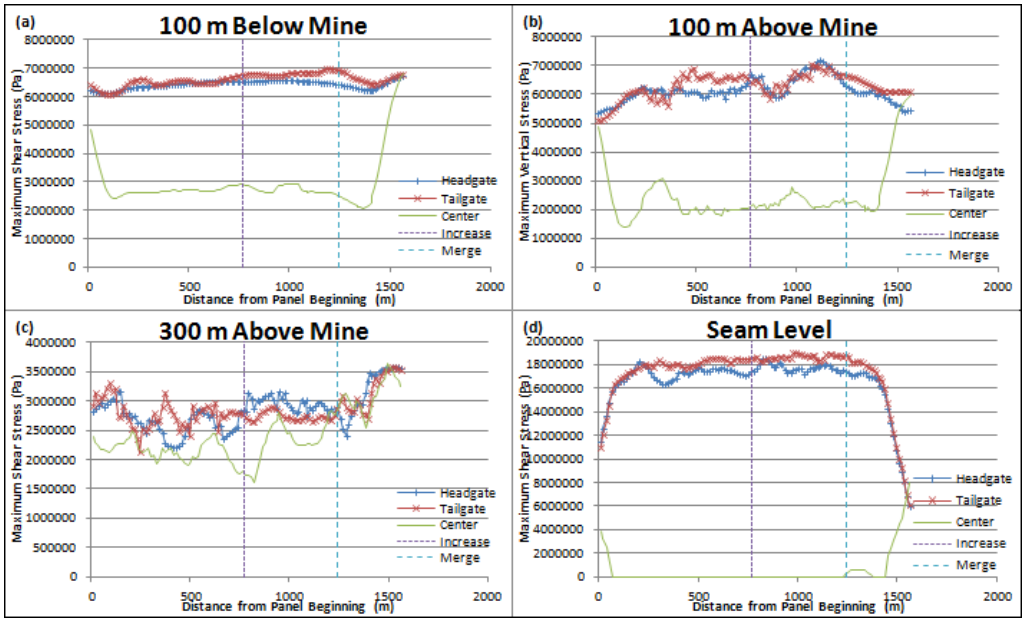

FIGURE 5.8 Maximum shear stress profiles from west to east on the headgate, tailgate, and center of the panel at (a) 100 m below mine level, (b) 100 m above mine level, (c) 300 m above mine level, and (d) at seam level. Vertical dashed lines indicate where the amount of seismicity increases and merges across the panel.

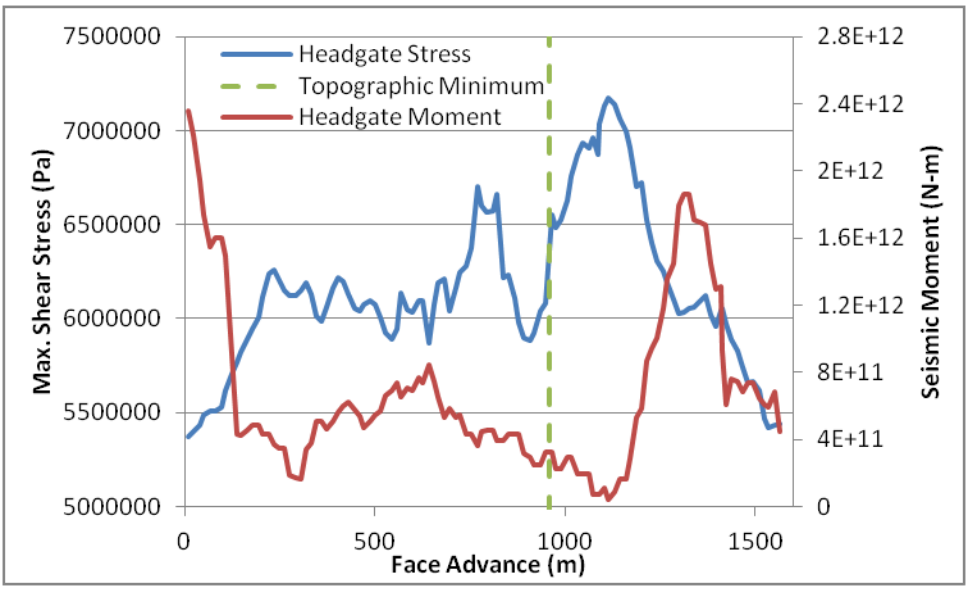

FIGURE 5.9 Shear stress and seismic moment on the headgate of Panel 13

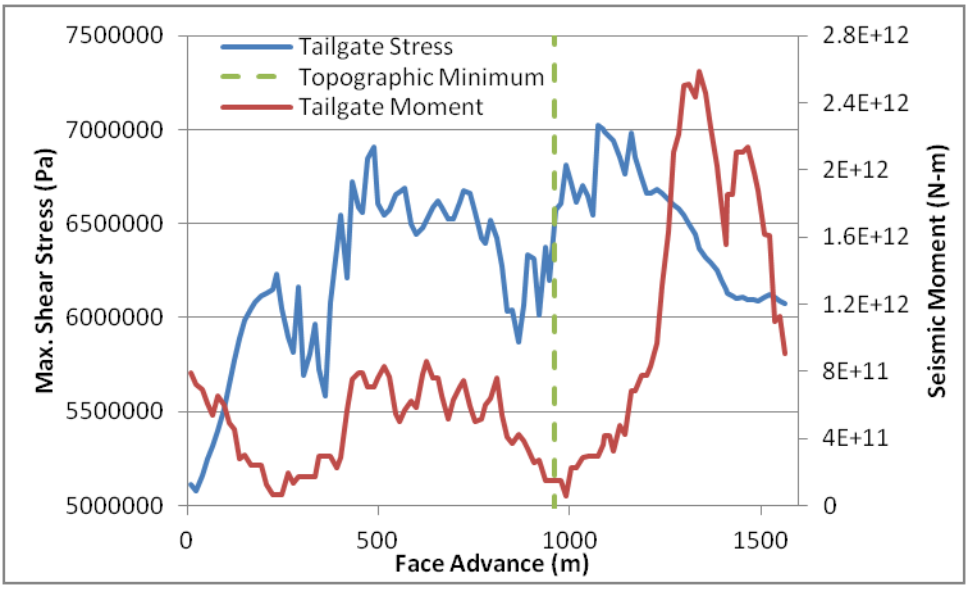

FIGURE 5.10 Shear stress and seismic moment on the tailgate of Panel 13

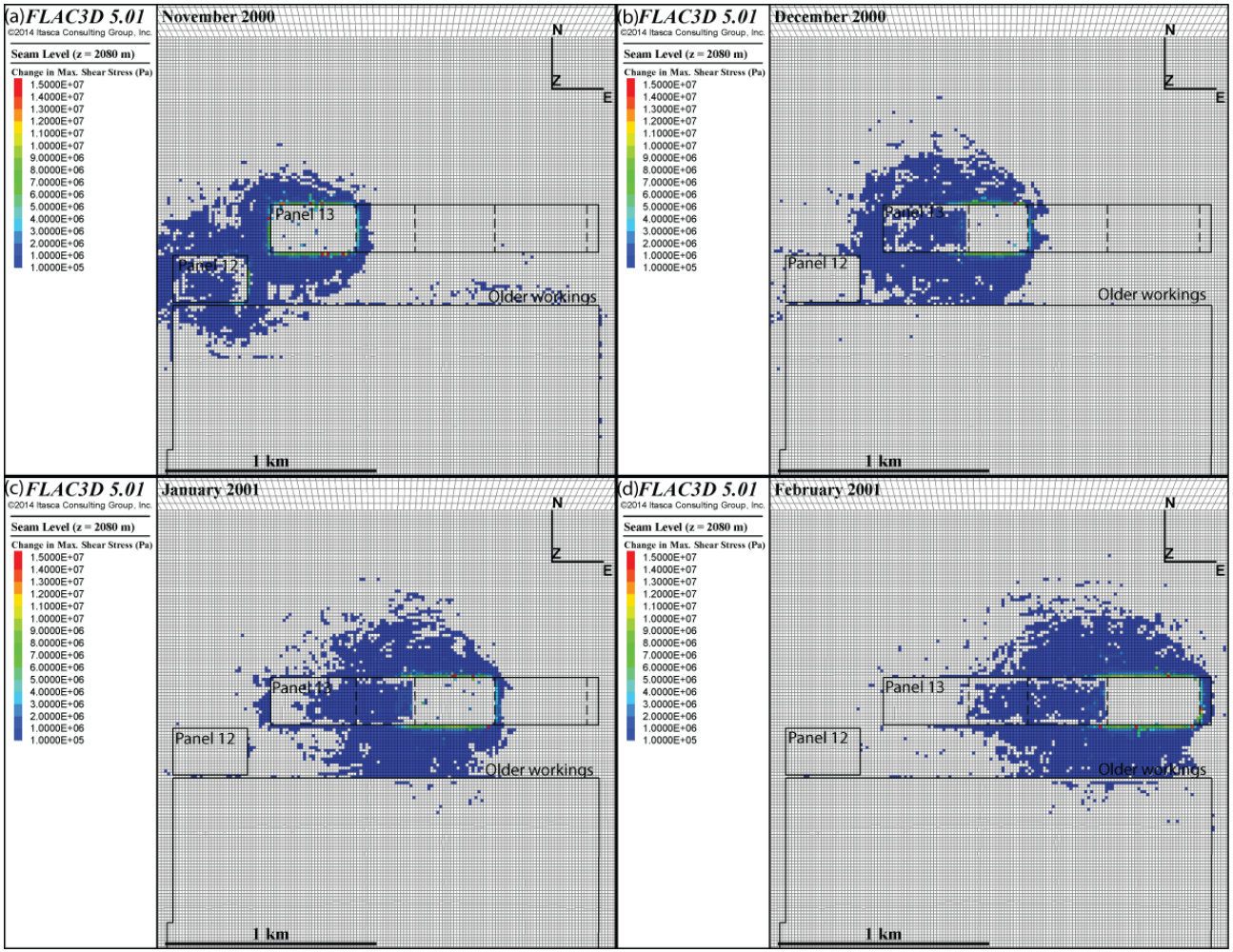

FIGURE 5.11 Seam-level plots illustrating the change in maximum shear stress caused by the excavation of material over one-month periods during mining of Panel 13. Colored areas denote a positive stress change greater than 0.1 MPa. Dashed lines delineate the excavation sections for Panel 13.

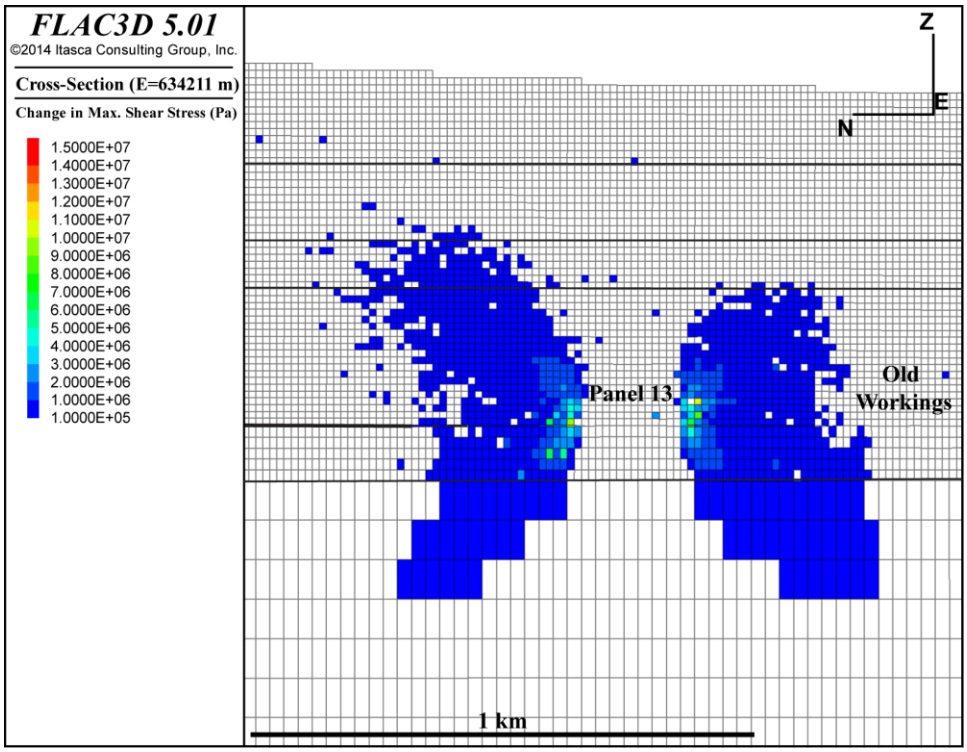

FIGURE 5.12 Cross-section plot illustrating the change in maximum shear stress around Panel 13. Colored areas denote a positive stress change greater than 0.1 MPa. Horizontal black lines delineate changes in the stratigraphic column.

6. CONCLUSIONS AND RECOMMENDATIONS

6.1. Conclusions

The objective of this study was to develop a *FLAC*^{3D} model of the TMM to identify failed zones and high stress areas around the mine workings. These areas were compared with the locations and energy of MIS recorded during the mining of Panel 13 to determine if there are correlations between these parameters. High stress areas were found to occur on the gateroads with a trend of increasing stress toward the east side of the modeled workings. The high stress areas do correspond to the locations of the seismicity, though there are some aspects of the seismicity that the model cannot fully explain. One feature of the seismicity that the model does not explain is the cluster at the end of the panel, which is thought to have been caused by factors that were not included in the model such as near-seam geology or the presence of older workings to the east. The model also cannot account for the absence of floor events and indicates there should be an approximately equal number of events in the roof and floor. The reason for the difference is unclear, but it indicates that the stresses alone are not a sufficient indicator of the potential for MIS.

The failed zones in the model were compared with the locations and moments of the seismicity recorded on Panel 13. The failed zones did not correlate well with either the locations or the moments of the seismicity and cannot account for the increase in the seismicity rate at the east end of the panel. The main reason for this lack of correlation is likely that the failures in the model do not distinguish between zones that would fail

seismically or aseismically. It is possible that the relation between these parameters could be improved by including other factors such as near-seam geology or by better accounting for the presence of joints.

The maximum shear stress and change in maximum shear stress are the parameters that were examined in this study that seem to provide the best relation to the locations of the MIS. The maximum shear stress more clearly illustrates the increasing stress at the east end of the panel and also shows increased stress on the tailgate relative to the headgate, consistent with more seismicity on the tailgate. Additionally, the shear stress lines up with the seismic moment such that areas of increased seismic moment occur after peaks in the shear stress, which is consistent with the seismicity being related to de-stressing of the rock mass. The change in maximum shear stress is a useful parameter because it delineates the extent of stress perturbations caused by the mining activity. If the events were to have primarily shear failure mechanisms, then it is logical that the shear stress would be a better indicator of the potential for seismicity.

An inherent flaw with the model developed in this study is the representation of joints. The SUBI constitutive model uses a nonphysical method for adjusting the stresses of zones with failed joints, causing an unrealistically low stress in the zone after failure. The model also does not account for the anisotropy of the elastic moduli as a result of jointing. The errors introduced by this constitutive model are further compounded by the use of a coarse grid, causing a single joint set to dominate the model when it should have a much smaller presence. As a result of the flaws with the representation of joints, the stresses in zones with joints tend to be lower than reality, causing an error in the stresses of approximately 12.5%.

The results of this thesis are not conclusive enough to predict where seismicity will occur based on the stresses in the model, but the results are still useful. In addition to showing that there is a relationship between the stresses and seismicity, the model also demonstrates that it is possible to conduct a mine-wide analysis using *FLAC*^{3D}. A significant challenge in conducting a mine-wide analysis is that it requires modeling a large region (6 km × 6 km × 1.5 km) while the coal seam is very thin (< 3 m). This model illustrates that through careful generation of the grid and selection of the parameters that define when the model reaches equilibrium, it is possible to obtain both practical runtimes and reasonable results. The results of the model could also serve as a foundation for future research on the seismicity at this mine.

6.2. Recommendations

The model presented in this thesis is a good starting point for modeling the MIS recorded at the TMM. There are a number of ways that this model could be improved in future work. Factors that are thought to have influenced the seismicity that were not represented in this model should be included in future modeling efforts. These factors include changes in near-seam geology, the mine workings located to the east of Panel 13, and entries around the currently modeled panels.

Another improvement to this model would be the use of a constitutive model that is better able to account for the presence of jointing in the rock mass. One difficulty with an equivalent continuum jointing model is being able to accurately reflect the behavior of the joints. The Ubiquitous-Joint model for *FLAC*^{3D} is flawed because it does not account for anisotropy caused by jointing and it biases the stresses in a zone experiencing joint failure. There are several models that have been developed that are a step closer to more

realistically representing joints in *FLAC*^{3D}. One such model is a user-defined constitutive model for *FLAC*^{3D} that accounts for anisotropy in the elastic moduli caused by three fully-persistent joint sets (Agharazi et al. 2012). This model is still based on the Ubiquitous-Joint model and has similar problems with nonphysical stress adjustments after failure. Another alternative could be to use a discontinuum method or to calibrate the Ubiquitous-Joint model using a discontinuum code (Sainsbury et al. 2008). A finer grid could also be used to make sure that the different joint sets are adequately represented.

Finally, future work should focus on examining other parameters that may be more indicative of the potential for seismicity. While this study and others have shown that there are weak relationships between shear stress and MIS, the relationships are insufficient to determine areas in a mine that may be more likely to experience seismicity. Other parameters that may be better related to seismicity include the excess shear stress, Coulomb failure stress changes, or energy release in the model.

REFERENCES

Agharazi, A., Martin, C.D., Tannant, D.D. 2012. A three dimensional equivalent continuum constitutive model for jointed rock masses of up to three joint sets. *Geomechanics and Geoengineering: An Int. J*. 7(4): 227–238. Accessed September 2013. doi 10.1080/17486025.2012.714476.

Arabasz, W.J., Nava, S.J., McCarter, M.K., and Pankow, K.L. 2002. *Ground Motion Recording and Analysis of Mining-Induced Seismicity in the Trail Mountain Area, Emery County, Utah*. Final report to State of Utah School and Institutional Trust Lands Administration. Salt Lake City, UT: University of Utah Seismograph Stations.

Arabasz, W.J., Nava, S.J., McCarter, M.K., Pankow, K.L., Pechmann, J.C., Ake, J., and McGarr, A. 2005. Coal-mining seismicity and ground-shaking hazard: A case study in the Trail Mountain area, Emery County, Utah. *Bull. Seismol. Soc. Am.* 95(1):18–30. Accessed November 2012. doi 10.1785/0120040045.

Badr, S., Ozbay, U., Keiffer, S., and Salamon, M. 2003. Three-dimensional strain softening modeling of deep longwall coal mine layouts. In *FLAC and Numerical Modeling in Geomechanics.* Lisse: Swets and Zetlinger. pp. 233–239.

Boltz, M. S., Pankow, K.L., and McCarter, M.K. 2012. Relocating mining-induced seismicity at the Trail Mountain Mine. In *Proc. of the 31st Int. Conf. on Ground Control in Min*. Morgantown, WV, July 31–August 2.

Boltz, M.S., Pankow, K.L., and McCarter, M.K. 2014. Fine details of mining-induced seismicity at the Trail Mountain Mine using modified hypocentral relocation techniques. *Bull. Seismol. Soc. Am.* 104(1). Accessed February 2014. doi 10.1785/0120130011.

Cohee, B.P., and Beroza, G.C. 1994. A comparison of two methods for earthquake source inversion using strong motion seismograms. *Annali di Geofisica*. 37(6):1515–1538.

Cundall, P., Gomez, P., Lorig, L. Pierce, M., Sainsbury, D., Young, P. and Napier, P. 2005. *Caving Mechanics Task 1 Scoping Study*. Report to the International Caving Study, ICG052292-1-8.

Doelling, H.H. 1972. *Central Utah Coal Fields: Sevier-Sanpete, Wasatch Plateau, Book Cliffs and Emery.* Salt Lake City, UT: Utah Geological and Mineralogical Survey.

Ellenberger, J.L., and Heasley, K.A. 2000. Coal mine seismicity and bumps: historical case studies and current field activity. In *Proc. of the 19th Int. Conf. on Ground*

Control in Min. Edited by S.S. Peng and C. Mark. Morgantown, WV: West Virginia University. pp. 112–120.

Gibowicz, S.J. 2009. Seismicity induced by mining: Recent research. *Adv. in Geophys.* 51:1–53. Accessed May 2012. doi 10.1016/S0065-2687(09)05106-1.

Gibowicz, S.J. and Lasocki, S. 2001. Seismicity induced by mining: Ten years later. *Adv. in Geophys.* 44: 39–181. Accessed September 2012. doi 10.1016/S0065-2867(00)80007-2.

Iannacchione, A.T., and Zelanko, J.C. 1995. Occurrence and remediation of coal mine bumps: A historical review. In *Mechanics and Mitigation of Violent Failure in Coal and Hard-Rock Mines: U.S. Bureau of Mines Special Publication 01-95.* pp. 27–67.

Itasca Consulting Group. 2013a. *FLAC3D: Fast Lagrangian Analysis of Continua in 3 Dimensions.* User's Guide. Minneapolis, MN: Itasca Consulting Group Inc.

Itasca Consulting Group. 2013b. *FLAC3D: Fast Lagrangian Analysis of Continua in 3 Dimensions.* Theory and Background. Minneapolis, MN: Itasca Consulting Group Inc.

Itasca Consulting Group. 2013c. *FLAC3D: Fast Lagrangian Analysis of Continua in 3 Dimensions.* Constitutive Models. Minneapolis, MN: Itasca Consulting Group, Inc.

Johnston, J.C. 1992. Rockbursts from a global perspective. In *Induced Seismicity*. Edited by P. Knoll. Balkema, Rotterdam. pp. 63–78.

Jones, R.E. 1994. Investigation of sandstone escarpment stability in the vicinity of longwall mining operations. M.S. thesis, University of Utah, Salt Lake City, UT.

Karabin, G.J., and Evanto, M.A. 1994. Experience with the boundary element method of numerical modeling as a tool to resolve complex ground control problems. In *Proc. of the 13th Int. Conf. on Ground Control in Min.* Edited by S.S. Peng and C.T. Holland. Morgantown, WV: West Virginia University. pp. 201–213.

Kulatilake, P.H.S.W., Wang, X., and Song, W.D. 2013. Three-dimensional ground stability study around a mine tunnel in a highly discontinuous rock mass under significant in situ stress. In *Proc. of the 32nd Int. Conf. on Ground Control in Min.* Morgantown, WV, July 30–August 1.

Luo, X., Hatherly, P. and Gladwin, M. 1998. Application of microseismic monitoring to longwall geomechanics and safety in Australia. In *Proc. of the 17th Int. Conf. on Ground Control in Min.* Morgantown, WV, August 4–6. pp. 72–78.

Maleki, H. 2005. *Control of Mining-Induced Seismicity through Mine Design Application of U.S. Experience and Numerical Modeling in the Cottonwood Tract.* Report

prepared for: School and Institutional Trust Lands Administration (SITLA). Salt Lake City, UT: Maleki Technologies, Inc.

Mark, C. 2012. Characteristics of coal bursts in the North Fork Valley of the Gunnison River Valley, Colorado. In *Proc. of the 31st Int. Conf. on Ground Control in Min.* Morgantown, WV, July 30–August 1.

McCarter, M.K., and McKenzie, J.D. 2002. Trail Mountain project—Mining engineering considerations for assessing maximum magnitude for seismic events. In *Ground Motion Recording and Analysis of Mining-Induced Seismicity in the Trail Mountain Area, Emery County, Utah.* W.J. Arabasz, S.J. Nava, M.K. McCarter, and K.L. Pankow. Salt Lake City, UT: University of Utah Seismograph Stations.

Mercer, R.A., and Bawden, W.F. 2005. A statistical approach for the integrated analysis of mine-induced seismicity and numerical stress estimates, a case study—Part I: Developing the relations. *Int. J. Rock Mech. Min. Sci.* 42(1):47–72. doi 10.1016/j.ijrmms.2004.07.006.

Mohamed, K.M. 2003. Design considerations for longwall yield pillar stability. Ph.D. dissertation, West Virginia University, Morgantown, WV.

Pappas, D.M. and Mark, C. 1993. *Behavior of Simulated Longwall Gob Material.* Report of Investigations 9458 U.S. Bureau of Mines.

Pariseau, W.G. 2007. *Design Analysis in Rock Mechanics*. Leiden, The Netherlands: Taylor and Francis/Balkema.

Pariseau, W.G. 2012. Finite element approach to caving in stratified, jointed rock masses. *Int. J. of Rock Mechanics and Min. Sci.* 53: 94–100. Accessed July 2013. doi 10.1016/j.ijrmms.2012.05.004.

Pariseau, W.G., Hustrulid, W., Swanson, S., and Van Sambeek, L. 1977. *Coal Pillar Strength Study: The Design of Production Pillars in Coal mines*. Final report to U.S. Bureau of Mines. Contract No. H 0242059. Salt Lake City, UT, University of Utah.

Pechmann, J.C., Arabasz, W.J., Pankow, K.L., Burlacu, R., and McCarter, M.K. 2008. Seismological report on the 6 August 2007 Crandall Canyon mine collapse in Utah. *Seis. Res. Lett.* 79(5): 620–636. Accessed May 2014. doi 10.1785/gssrl.79.5.620.

Pierce, M. and Board, M. 2010. *Development of a Three-Dimensional Numerical Modeling Environment for Caving and Stress Analysis of Longwall Mining.* Report to National Institute of Occupational Safety and Health, Spokane Research Laboratory, NIOSH 2552-05. Minneapolis, MN: Itasca Consulting Group.

Ryder, J.A. 1987. Excess shear stress in the assessment of geologically hazardous situations. *J. S. Afr. Inst. Min. Metall.* 88(1): 27–39.

Sainsbury, B. 2012. A model for cave propagation and subsidence assessment in jointed rock masses. Ph.D. thesis. University of New South Wales, Sydney, Australia.

Sainsbury, B., Pierce, M.E., and Mas Ivars, D. 2008. Analysis of caving behaviour using a synthetic rock mass-ubiquitous joint rock mass modeling Technique. *In Proc. 1st Southern Hemisphere International Rock Mechanics Symposium*, Perth, Australia, September 6–19. pp. 243–253.

Salamon, M.D.G. 1990. Mechanism of caving in longwall coal mining. In *Rock Mechanics Contributions and Challenges: Proc. of the 31st US Symposium on Rock Mechanics*, Golden, CO. Edited by W. Hustrulid and G.A. Johnson. Balkema, Rotterdam.

Senfaute, G., Al-Heib, M., Josien, J.P., and Noirel, J.F. 2001. Detection and monitoring of high stress concentration zones induced by coal mining using numerical and microseismic methods. In *Rockbursts and Seismicity in Mines.* Dynamic rock Mass Response to Mining. Edited by G. van Aswegen, R.J. Durrheim, and W.D. Ortlepp. South African Inst. Min. Metal, Johannesburg. pp. 453–456.

Singh, M.M., and Kendorski, F.S. 1981. Strata disturbance prediction forming beneath surface water and waste impoundments. In *Proc. 1st Conf. on Ground Control in Min.* pp. 76–89.

Stein, R.S. 1999. The role of stress transfer in earthquake occurrence. *Nature*. 402: 605–609. Accessed March 2014. doi 10.1038/45144.

Spottiswoode, S.M., and McGarr, A. 1975. Source parameters of tremors in a deep-level gold mine. *Bull. Seism. Soc. Amer.* 65:93–112.

Spottiswoode, S.M., Linzer, L.M., and Majiet, S. 2008. Energy and stiffness of mine models and seismicity. In *Proc. 1st South. Hemisphere Rock Mechanics Symposium.* Edited by Y. Potvin, J. Carter, A. Dyskin, and R. Jeffrey. Australian Centre for Geomechanics, Nedlands. pp. 693–707.

Wang, X., Kulatilake, P.H.S.W., Song, W.D. 2012. Stability investigations around a mine tunnel through three-dimensional discontinuum and continuum analyses. *Tunnelling and Underground Space Technol*. 32: 98–112. Accessed September 2013. doi 10.1016/j.tust.2012.06.003.

Wiles, T. 2005. Rockburst prediction using numerical modelling—realistic limits for failure prediction accuracy. In *Rockbursts and Seismicity in Mines*. Controlling Seismic Risk. Edited by Y. Potvin and M. Hudyma. Australian Centre for Geomechanics, Nedlands. pp. 57–63.

Wilson, P.E., and Kneisley, R.O. 1995. Mapping stress changes with microseismics for ground control during longwall mining. In *Mechanics and Mitigation of Violent*

Failure in Coal and Hard-Rock Mines: U.S. Bureau of Mines Special Publication 01-95. pp. 91–103.

Zoback, M.L., Zoback, M.D., Adams, J., Assumpção, M., Bell, S., Bergman, E.A., Blümling, P., Brereton, N.R., Denham, D., Ding, J., Fuchs, K., Gay, N., Gregersen, S. Gupta, H.K., Gvishiani, A., Jacob, K., Klein, R., Knoll, P., Magee, M., Mercier, J.L., Müller, B.C., Paquin, C., Rajendran, K., Stephansson, O., Suarez, G., Suter, M., Udias, A., Xu, Z.H., and Zhizhin, M. 1989. Global patterns of tectonic stress. *Nature*. 341: 291–298. Accessed March 2014. doi 10.1038/341291a0.